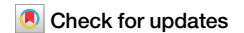


<https://doi.org/10.1038/s42003-025-08991-z>

Heme processing in the malaria parasite, *Plasmodium falciparum*: a time-dependent basal-level analysis

Larnelle F. Garnie¹, Timothy J. Egan^{1,2} & Kathryn J. Wicht^{1,2}✉

Malaria is a deadly disease for which therapeutic options are threatened by the rise of antimalarial resistance. Inhibiting the formation of hemozoin (the product of heme detoxification) in the digestive vacuole (DV) is the mechanism of action of numerous antimalarial drugs, including those in development as new therapies. This drug target remains attractive as hemozoin is an abiotic and non-mutable molecule, unique to the parasite. The underlying parasite biology of the heme detoxification pathway is complex and requires a deeper understanding. This study focuses on the DV of *Plasmodium falciparum*, utilizing confocal microscopy, immunofluorescence, immunoblotting and cellular fractionation techniques to study its native state over time. Using parameters such as the uptake into and growth of the DV, relative abundance of plasmepsins (PMs) I and IV as well as basal levels of hemoglobin, heme and hemozoin, it was found that DV physiology in chloroquine (CQ)-sensitive NF54 follows three distinct developmental phases: the lag-type growth (20 to 28 h), rapid growth phase (28 to 40 h) and the plateau (40 to 48 h). These phases hold specific characteristics with respect to the investigated parameters. In addition, key differences between CQ-sensitive NF54 and CQ-resistant Dd2 parasites were observed.

Plasmodium falciparum parasites cause the most virulent form of malaria, a disease that infected 263 million people in 2023 and resulted in 597,000 fatalities. Strikingly, 94% of these cases and fatalities occurred in the World Health Organization (WHO) African Region¹. Currently, the WHO-recommended treatment for uncomplicated blood-stage malaria is the use of artemisinin-based combination therapies (ACTs), in which a fast-acting artemisinin derivative is administered in combination with a slow acting partner compound^{1–3}. However, concerns are rising over the continued efficacy of ACTs, owing to reports of partial artemisinin resistance in East Africa⁴.

Some of the widely used ACT combinations such as artesunate-amodiaquine, artesunate-mefloquine, artesunate-pyronaridine, artemether-lumefantrine, and dihydroartemisinin-piperaquine contain partner drugs that target essential processes within the heme detoxification pathway of the parasite^{2,3}. Furthermore, many recent studies have identified new classes of antiplasmodium compounds that therapeutically act on this pathway^{5–10}.

During the asexual blood stage (ABS), the symptomatic stage of a *P. falciparum* infection, parasites ingest and degrade hemoglobin resulting in the release of cytotoxic heme, which is subsequently detoxified through incorporation into a crystal called hemozoin. Inhibiting hemozoin

formation remains an attractive approach, in spite of wide-spread drug resistance to the classical hemozoin formation inhibitor, chloroquine (CQ), given that the resistance mechanism of CQ involves drug-specific efflux from the DV by the chloroquine resistance transporter, *PfCRT*. Notably, no changes in the process of hemozoin formation itself have been observed in strains resistant to hemozoin formation inhibitors. Indeed, many hemozoin formation inhibitors are active against the CQ-resistant *Pf* strain, Dd2, which harbours eight mutations in *PfCRT* compared with the wild-type CQ-sensitive NF54 strain^{11–13}.

Previous studies have shown that hemoglobin uptake commences during the ring stage through the formation of cytosomal invaginations containing hemoglobin^{14–18}. It has been suggested that these hemoglobin-filled vesicles then coalesce to form the central DV compartment¹⁶. Although this is the most widely accepted uptake route, other uptake mechanisms such as the “Big Gulp” have also been suggested¹⁸. Hemoglobin is then digested by a cohort of proteases localized to the DV^{19–21}. The aspartic proteases plasmepsin (PM) I, II, III (also known as histoaspartic protease) and IV, as well as cysteine proteases falcipain 2 and 3, have been shown to be involved in the initial catabolism of hemoglobin^{20,22–25} to produce oligopeptides resulting in the release of the heme moiety²⁶. The oligopeptides are

¹Department of Chemistry, Faculty of Science, University of Cape Town, Rondebosch, Cape Town, South Africa. ²Institute of Infectious Diseases and Molecular Medicine, Faculty of Health Sciences, University of Cape Town, Observatory, Cape Town, South Africa. ✉e-mail: kathryn.wicht@uct.ac.za

further degraded by action of falcilysin, a zinc metalloprotein²⁷, dipeptidyl aminopeptidase 1 (DPAP 1)^{28,29}, and various aminopeptidases^{30–32}. The cytotoxic heme released through this catabolic process is then oxidized and incorporated into insoluble hemozoin crystals. This process is proposed to be lipid-mediated, although there may also be proteins, such as heme detoxification protein and lipocalin, involved³³. Interestingly, only 16% of amino acids produced from hemoglobin catabolism are used by the parasite³⁴. Instead, it has been postulated that hemoglobin is catabolized to create space for the parasite to grow and to maintain osmotic pressure within the RBC to prevent premature lysis^{35,36}.

Antimalarials including CQ, amodiaquine, mefloquine, pyronaridine, piperazine and lumefantrine have been shown to inhibit β -hematin (synthetic hemozoin) formation in extracellular assays, whereas only a subset of these have demonstrated inhibition of hemozoin formation in cell-based assays. For example, true inhibitors of hemozoin formation cause a dose-dependent increase in free heme in treated parasites with a corresponding decrease in hemozoin in the cell fractionation assay^{11,37,38}. On the other hand, some compounds such as mefloquine, only show a decrease in hemozoin without an increase in heme. This effect may result from the inhibition of hemoglobin endocytosis, leading to a reduction in the total amount of released heme and therefore, hemozoin³⁹.

These observations highlight the importance of whole-cell studies to inform the mode of action for compounds exerting their therapeutic effect within the DV. Furthermore, although specific steps within the heme detoxification pathway have been studied in the context of specific enzymes or drugs, a holistic view of the basal parasite biology underlying this pathway is required to better describe DV processes. For example, changes in the DV lumen volume, PM protein concentrations, and the basal levels of heme-containing species during ABS parasite growth have not been extensively probed.

Thus, here we show changes in the DV lumen growth, excluding the hemozoin crystals, over time in CQ-sensitive NF54 and CQ-resistant Dd2 strains using confocal microscopy, and a macromolecular probe called pHrodo™ red dextran. This probe fluoresces only at low pH and was used to selectively stain the acidic DV^{40–42}. This approach allowed for live-cell imaging, which requires minimal pre-processing of the samples and largely maintains cellular integrity. To our knowledge this is the first use of pHrodo™ in this context. Three parameters: DV lumen volume, uptake into the DV and concentration of pHrodo™ within the DV were measured. In addition, we examined the wild-type PM I and PM IV protein levels over the trophozoite to schizont life stage using immunoblotting and densitometry techniques. Finally, we show differences in the basal levels of hemoglobin, heme and hemozoin between the NF54 and Dd2 strains using a heme fractionation assay³⁷. A culmination of these parameters allows for a more holistic overview of the DV and heme detoxification pathway.

Results

Digestive vacuole studies

Volume. Culture clock standards for NF54 and Dd2 were constructed over a consecutive 24-h period. The cell count-normalized fluorescence channel 1 area (FL1-A), representative of SYBR™ Green, correlates with the DNA content which increases as the parasite ages. For all time-sensitive assays, the FL1-A standard histograms were overlaid with the experiment histograms, and the Giemsa-stained thin films compared to confirm parasite age (Fig. 1^{43,44}, Supplementary Figs. 1 and 2).

Red blood cell (RBC) ghosts were pre-loaded with pHrodo™ using hypotonic lysis and hypertonic resealing (Fig. 1). Parasites were then allowed to re-invade the loaded RBCs. Following the incubation period, Z-stacks of individual parasites were acquired on a confocal microscope (Figs. 1 and 2A, Supplementary Fig. 3) and these were analyzed in ImageJ to calculate the DV lumen volume (Fig. 2B)^{45–47}. Time 0/48 h and 0/46 h for NF54 and Dd2, respectively, were treated as the point at which the schizonts burst to release merozoites. At these time points, the remnant DV lumen is significantly reduced as shown in the schizont inset of Fig. 2B, where the hemozoin is tightly wrapped in the DV membrane. Therefore, on this basis,

the curve was arbitrarily extrapolated to the origin for both strains and to (48,0) and (46,0) for NF54 and Dd2, respectively. Previous studies have shown transmission electron microscopy (TEM) images similar to those shown in the insets of Fig. 2B^{48,49}.

The growth of the DV lumen between 0 and 36 h in NF54 most accurately fit a Gompertz growth curve (Fig. 2B)^{50,51}. The plateau of the curve within the NF54 dataset was not reached before the DV lumen began to decrease in size at 40 h. For simplicity in the text, this decrease in volume of the lumen space is described as the “collapse” of the DV lumen. Between 40 and 48 h the DV lumen collapsed following a linear regression. In Dd2, the life cycle more accurately followed a 46-h cycle, and the DV lumen expanded between 0 and 32 h, also according to the Gompertz growth curve. In this case, contrary to what was observed for NF54, the plateau was seen to begin near 32 h before the Dd2 DV lumen collapsed linearly between 36 and 46 h. In order to examine the relationship between the collapse of the lumen and schizogony, the number of nuclei in individual parasites was determined at peak lumen volume vs during the lumen collapse. It was found that, based on the Hoechst profile, at the 36 h peak in NF54, 11 out of 32 were diffused, 11 were multinuclear and the remainder singular. At the 32 h peak in Dd2, 3 out of 20 nuclei were diffused and the remainder singular. The diffuse profile is indicative of DNA replication and the beginning stages of schizogony. Furthermore, during the collapse in NF54, 14 out of 14 parasites imaged at 40 h contained greater than one nuclei, whereas in Dd2 at 36 h, 8 out of 15 were multinuclear with the remainder showing a diffuse profile. These data therefore indicated that the lumen collapse coincided with the appearance of schizonts at the relevant time points for each strain. Future studies spanning shorter intervals would be useful to more accurately ascertain the timing of the lumen collapse.

Uptake and concentration. In addition to studying the DV lumen volume, pHrodo™ was used to approximate the uptake into the DV via endocytosis. pHrodo™ was used as a proxy for hemoglobin on the basis that during the hypotonic lysis and hypertonic resealing of the RBCs, pHrodo™ was loaded into the RBC cytoplasm and was endocytosed as the parasite ingested the RBC cytosol. Using the “Analyze Particles” function in ImageJ^{45,46}, the background-corrected, integrated density over each Z-stack was calculated and averaged over all the samples for each time-point to determine the fluorescence intensity (Fig. 2C) within the DV.

It was found that the data trends for uptake into the lumen closely resemble those of DV lumen growth. Between 0 and 40 h in NF54, the uptake into the DV was shown to also follow Gompertz growth, corresponding with DV lumen growth (Fig. 2C). Furthermore, the collapse of the DV lumen between 40 and 48 h corresponds to a linear decrease in the amount of RBC cytosol taken up into the lumen. In contrast to the Gompertz growth curve fit to NF54 uptake, for Dd2 (Fig. 2C), a more flexible sigmoidal curve (variable slope) was fitted to the DV uptake between 0 and 32 h. Between 36 and 46 h, there was a linear decrease in the uptake into the lumen. The pHrodo™ concentration, calculated as the uptake averages divided by lumen volume, was found to be statistically constant over all timepoints in both NF54 and Dd2 (Fig. 2D).

PM I and IV protein analysis

Protein levels over time. Given the importance of the PMs in hemoglobin catabolism, PM I and PM IV were chosen as model enzymes for this study. It has been shown that these increase in abundance in aging parasites⁵², therefore the time-dependent levels in NF54 parasites, as a representative model strain, were examined in this study. As an internal control, the constitutively expressed endoplasmic reticulum chaperone binding immunoglobulin protein (BiP) was used as a proxy for changes in the total protein over the trophozoite to schizont stage^{53,54}. Immunoblots of parasite cell lysates were separated via 12% sodium dodecyl sulfate polyacrylamide gel electrophoresis (SDS-PAGE), transferred to PVDF membranes and probed with anti-PM I, anti-PM IV and anti-BiP antibodies (Fig. 3 and Supplementary Fig. 4A, B). Dd2 PM I and PM IV knockout (KO) lines were used as controls to confirm specificity of the

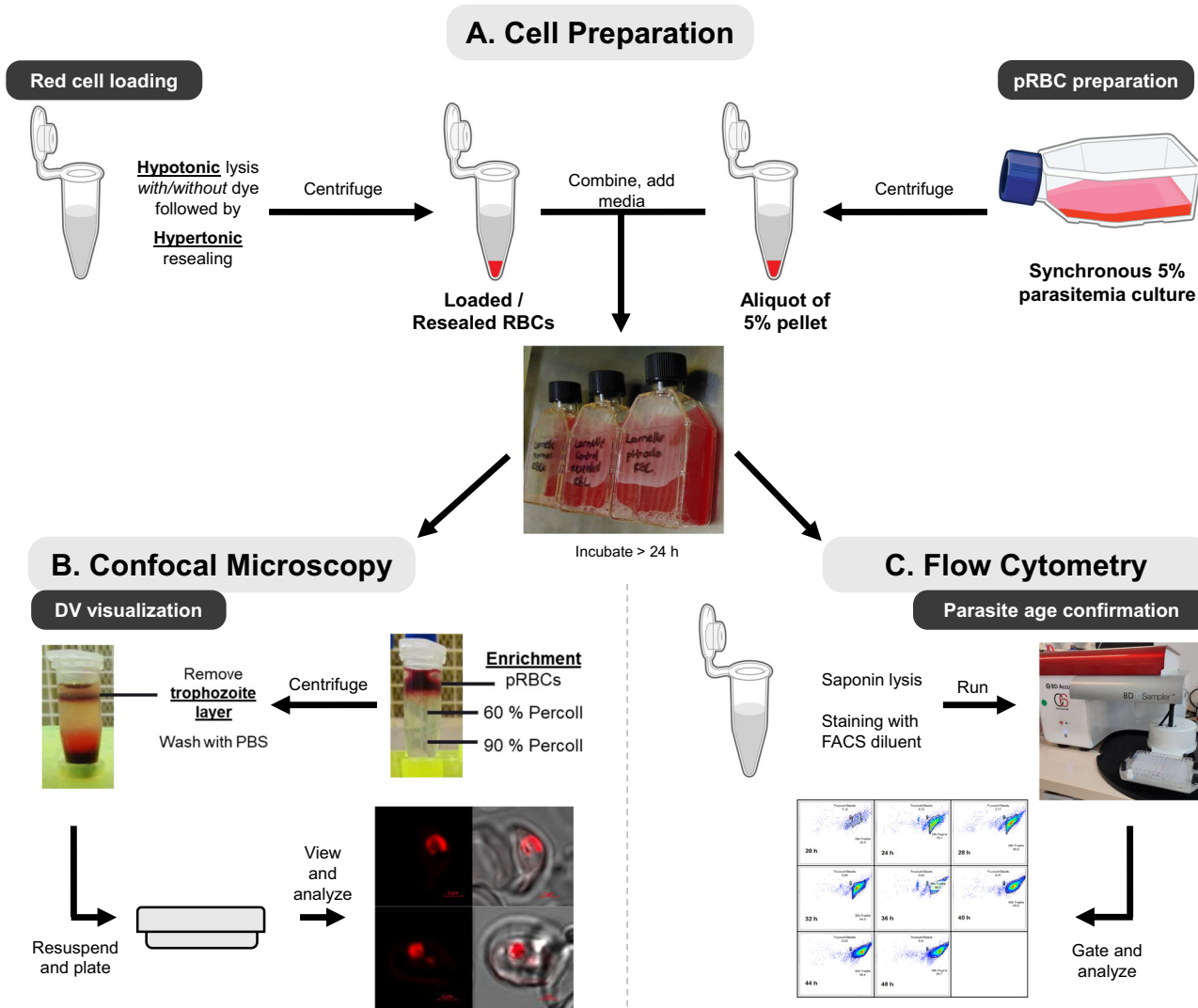


Fig. 1 | Method summary of confocal imaging and flow cytometry for NF54 parasites to determine the volume of and uptake into the DV lumen. A Cell preparation involved hypotonic lysis and hypertonic resealing of RBCs to produce resealed RBCs (with and without pHrodo). In addition, an aliquot of a 5% parasitemia culture was added to the resealed RBCs and media, followed by incubation at 37 °C for more than 24 h. B Purified trophozoite-containing pRBCs were obtained

through enrichment, resuspended, and plated in imaging dishes. Images were then acquired using confocal microscopy. C An aliquot of the pRBCs was saponin lysed, fixed, and stained in preparation for flow cytometry. The samples were run on a flow cytometer and the resultant populations gated and analyzed to confirm parasite age. Icons sourced from NIAID NIH BioArt^{43,44}.

antibodies⁵⁵. Densitometric analysis⁵⁶ of the protein levels per 50,000 parasites provided relative quantification of the three proteins and enabled the calculation of the relative amount of PM I and PM IV from 20 to 44 h (Fig. 3A, B). For both PM I and PM IV the calculated protein levels between 20 and 28 h remained at a similar level, after which there was a statistically significant increase from 28 to 32 h for both proteins. Between 32 and 44 h there was a gradual increase between consecutive timepoints with the levels reaching a plateau between 40 and 44 h.

The levels of BiP showed an overall increase from 20 to 44 h (Fig. 3C) with the levels between 20 and 28 h remaining steady. The increase from 28 to 44 h, however, followed a steeper trend than PM I and PM IV, with a statistically significant increase in the levels between 28 and 32 h, as well as 32 and 36 h. A plateau in the BiP levels was observed between 40 and 44 h. Overall, all three proteins show a general increase over the 24-h period examined.

Normalized protein levels. Given that the amount of all three proteins generally increases over the early trophozoite to mid schizont stage, it is plausible that the increase in PM I and PM IV expression may be

accounted for by an increase in total protein per parasite as the trophozoite expands. Therefore, to account for total protein increase, the PM I and PM IV protein bands were normalized to BiP to show changes in the relative amounts of PM I and PM IV with respect to the total protein in the parasite (Fig. 3D). In doing so, a steady expression relative to BiP was observed across timepoints, except for a small but statistically significant difference for PM I between 32 and 36 h. Therefore, within the limitations of the immunoblotting technique, the combination of the observed trends suggest that PM I and PM IV expression increases over the trophozoite to schizont stage in accordance with a universal cellular increase in protein levels as the parasite grows.

However, the time-dependent concentration of these enzymes in the DV is more insightful than absolute amounts with respect to the process of hemoglobin degradation within the DV. Therefore, the relative levels of PM I and PM IV were overlaid and compared to DV lumen growth (Supplementary Fig. 4C, D) as well as the uptake into the DV (Supplementary Fig. 4E, F). For both PM I and PM IV, the increase in relative protein abundance from 20 to 40 h corresponded with the increasing DV lumen volume and increase in uptake. The 44 h timepoint showed the largest

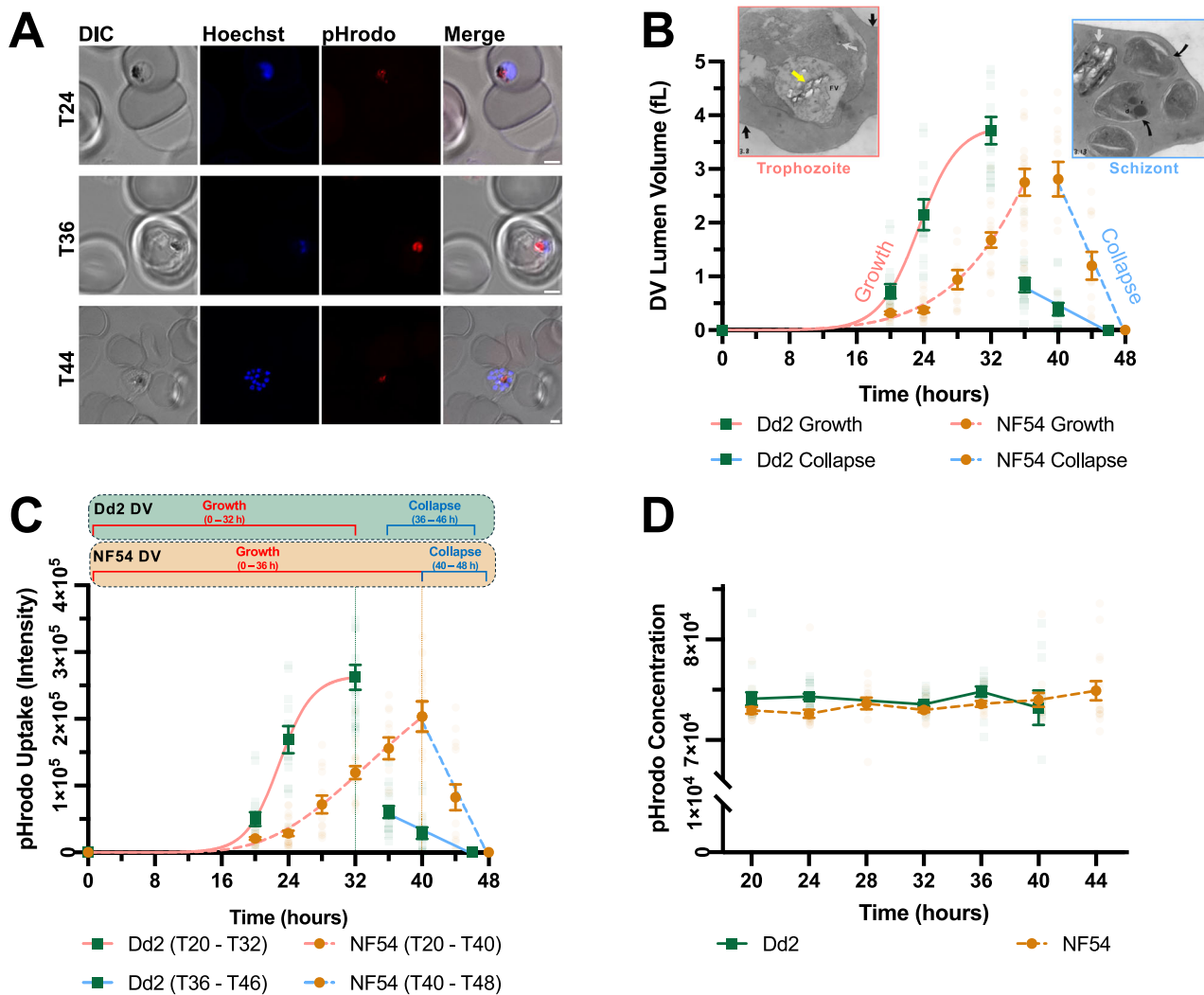


Fig. 2 | Digestive vacuole lumen volumetric and uptake analysis in *Pf* parasites (Dd2 and NF54) using confocal microscopy. Parasites were allowed to re-invade RBCs pre-loaded with pHrodo™-dextran red and imaged using the Z-stack functionality of an LSM 880 Airyscan confocal microscope (Zeiss). **A** A single Z-stack slice of representative individual RBCs infected with NF54 parasites at various timepoints (stipulated on image). Hoechst (blue) stains the DNA while pHrodo™ (red) selectively stains the DV. All scale bars represent 2 μm. **B** Growth of the DV lumen in *Pf* parasites as determined using the 3D Objects Counter (3D OC) calculation in ImageJ^{45–47}. Growth and collapse curves obtained for both strains were plotted on the same axis. Gompertz growth curves were fitted to the growth of the lumen and exhibited an $r^2 > 0.99$ for both strains, while linear regression analysis of the collapse exhibited an $r^2 > 0.98$ for both strains. Insets: TEM image of a trophozoite, magnification $\times 32,500$, DV is labeled as FV (food vacuole). Yellow arrow = hemozoin crystals, black arrow = knobs on RBC membrane, white arrow = dense granules. TEM image of a late schizont stage, magnification $\times 32,500$. Black arrows =

separated merozoites, white arrow = redundant DV in which the hemozoin is “shrink-wrapped” in the DV membrane and devoid of any lumen space, r = rhoptries, d = dense granules. Images produced from unpublished data taken from Honors dissertation of Dr Joanne Egan with permission. **C** The uptake of pHrodo™ into the DV lumen of *Pf* parasites measured by absolute fluorescence intensity using the “Analyze Particles” (AP) function in ImageJ. The phases of DV lumen growth and collapse are shown on the graphs for reference and the endpoint of the DV lumen growth is shown as a dotted line. NF54 uptake data was fitted to a Gompertz growth curve with $r^2 > 0.99$ for $0 \leq x \leq 40$ and a linear regression with $r^2 > 0.98$ for $40 \leq x \leq 48$. Dd2 uptake data was fitted to a sigmoidal growth curve (variable slope) with $r^2 > 0.99$ for $0 \leq x \leq 32$ and a linear regression with $r^2 > 0.97$ for $36 \leq x \leq 46$. **D** The concentration of pHrodo™ within the DV in arbitrary units, calculated as intensity divided by DV lumen volume. For each data point in graphs $n \geq 14$, where n represents the number of individual parasites (from two independent biological repeats; error bars indicate SEM).

difference between both PM I and PM IV levels and the DV lumen volume and uptake, respectively, compared to the other timepoints, given that the DV had already collapsed substantially. As a representation of PM concentrations, the levels of PM I and PM IV were then normalized to the DV lumen growth (Fig. 3D), where constant concentrations were observed between 28 and 40 h, but larger values obtained for the 20 to 28 h, and 44 h timepoints.

Immunofluorescence assays (IFA). To explore why there appeared to be a large concentration of PM I and PM IV at 44 h, immunofluorescence assays were performed on mixed age trophozoites and schizonts, the latter were identified by their multinuclear state. Given that the anti-CRT

(mouse) and anti-PM I (rabbit) antibodies were raised in different animals, these could be used in the same experiment and therefore, anti-CRT was used as a DV marker as PfCRT localizes to the DV membrane. On the contrary, anti-PM IV (mouse) could not be used in the same experiment as anti-CRT (mouse) and therefore, the hemozoin was used as an indicator of DV location. Briefly, NF54 parasites were fixed, permeabilized and stained with PM I and PM IV antibodies followed by the appropriate secondary fluorescent antibody. Parasites were then visualized with an LSM900 confocal microscope, whereupon PM I and PM IV were found to localize within the DV in both the trophozoite and schizont stage (Fig. 3E, F). This was observed by the colocalization of PM I and PM IV with hemozoin and, in the case of PM I, by the surrounding PfCRT signal. This

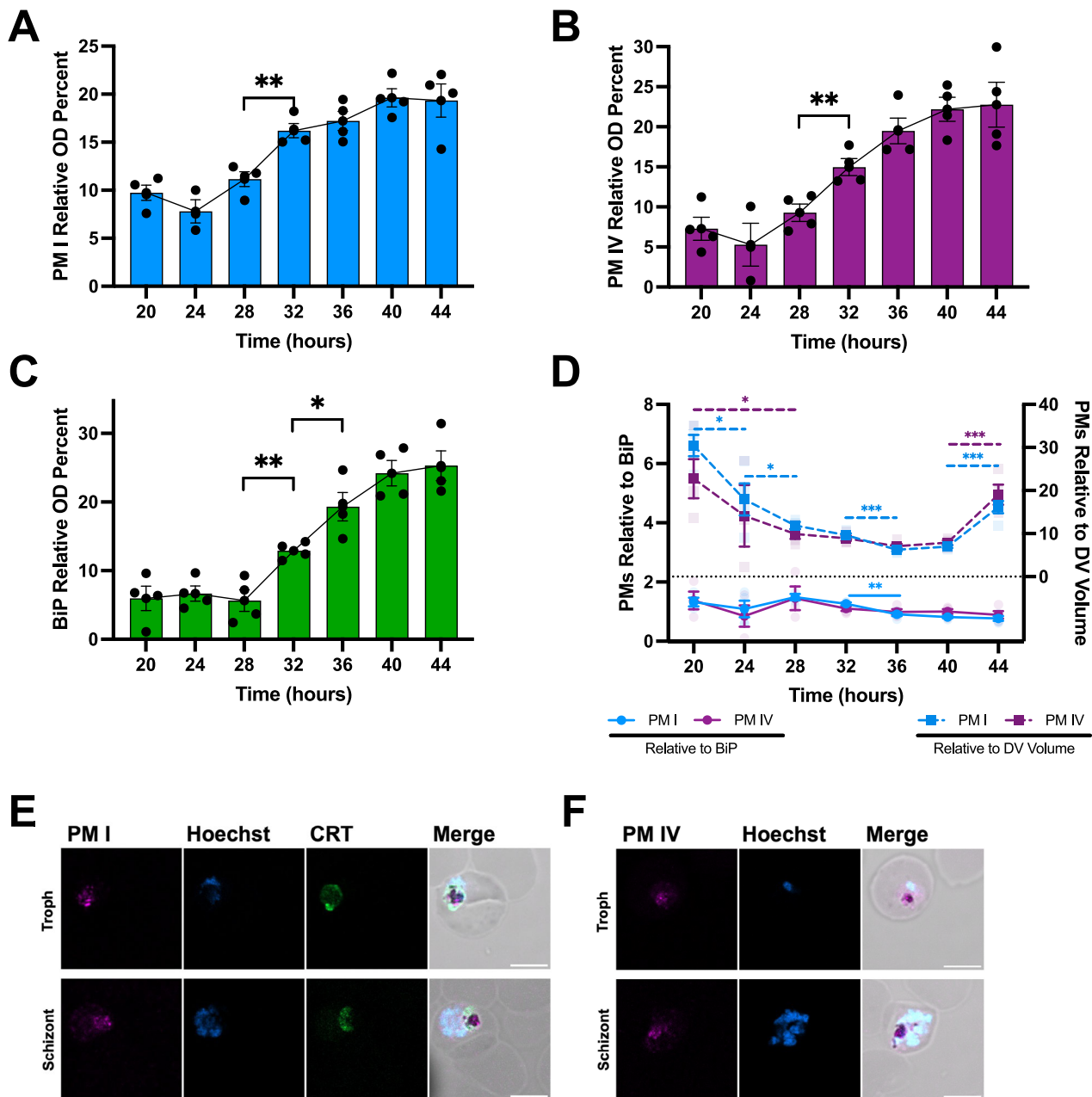


Fig. 3 | Immunoblot and immunofluorescence analysis of hemoglobinas PM I and IV. Cell lysates obtained from ~50,000 parasites (as determined by flow cytometry) over the trophozoite to schizont phase were separated on a 12% SDS-PAGE and then transferred to a PVDF membrane. The membranes were probed with anti-PM I (rabbit, 1:10,000), anti-PM IV (mouse, 1:5000) and anti-BiP (rabbit, 1:10,000) antibodies. Following chemiluminescent detection of the immunoblot signals, densitometric analysis of the blots were carried out using ImageJ as previously described⁵⁶. **A–C** The relative amounts of PM I, PM IV and BiP, respectively. The y-axes are represented as relative OD percentages in arbitrary units. **D**. Relative

amounts of PM I and PM IV normalized to BiP (left y-axis, circles, solid line) or DV lumen volume shown in Fig. 2C (right y-axis, squares, dotted line). Significance levels were calculated using two-tailed, unpaired student's t-tests where $N = 3-4$ for each timepoint ($*p < 0.05$; $**p < 0.01$, $***p < 0.001$, error bars indicate SEM). **E** Immunofluorescence images of representative NF54 parasites probed with Hoechst stain (blue), anti-PM I (rabbit, 1:2000, purple) and anti-CRT (mouse, 1:300, green) antibodies. **F** Immunofluorescence images of representative NF54 parasites probed with Hoechst stain (blue) and anti-PM IV (mouse, 1:500, purple) antibodies. Scale bars represent 5 μm .

indicates that the most likely explanation for the collapse of the DV lumen is that, as the metabolism of the parasite slows down and energy is diverted into making merozoites, the hemozoin crystals grow to take up most of the space in the DV. Although the IFA does not differentiate between intact protein and those in the process of being broken down, it is likely more energetically favorable to package the remaining PM I and PM IV proteins in the residual DV body and simply leave it behind when the schizont bursts to release merozoites. Thus, the higher relative concentration of the PMs at 44 h appears to be a byproduct of the shrinking

DV lumen concentrating the enzymes in the remaining space, rather than a functional requirement.

Basal levels of the heme-containing species

Percentage and absolute levels. To probe the relationships between the DV lumen or proteases, and the basal levels of hemoglobin, heme and hemozoin, parasites were subjected to a time-dependent heme fractionation assay over a 24-h period. Following incubation and harvesting of saponin-lysed trophozoites, the fractionation process involves the use of appropriate buffers or solvents to solubilize the various heme-containing

fractions. Therefore, first the hemoglobin fraction is solubilized using an aqueous buffer before centrifugation, where the solubilized fraction is harvested leaving the insoluble fractions in the pellet. Following the addition of a sodium dodecyl sulfate (SDS) and aqueous pyridine solution for the free heme fraction, or NaOH for the hemozoin fraction, these steps are repeated sequentially allowing each heme-containing fraction to be individually liberated and harvested. Taking advantage of the heme-pyridyl complex that is formed when pyridine is added to each soluble fraction, the heme content of each fraction is quantified using UV-vis spectroscopy. This is then converted to the amount of iron (Fe) using a heme standard curve. An additional parameter available from this data is the percent of each heme species relative to the others.

The percentage levels for each heme-containing species in NF54 parasites remained stable over the entire 24-h period resulting in an overall mean percent for hemoglobin ($1.1 \pm 0.1\%$), heme ($7.9 \pm 0.2\%$) and hemozoin ($91 \pm 0.2\%$) across all timepoints (Fig. 4A, C). The absolute levels of hemoglobin, heme and hemozoin and the total Fe per parasite allow for direct comparisons between each heme-containing species, with those of hemoglobin Fe spanning a narrow range from 0.28 ± 0.02 fg/cell (20 h) to 1.3 ± 0.2 fg/cell (44 h). In contrast, the heme, hemozoin and total Fe levels appear to follow an exponential increase (Fig. 4E, G), although the rate of this increase slows for both hemozoin and total Fe between 36 and 44 h. Given that hemozoin makes up approximately 90% of the total Fe, it is unsurprising that the trends for these two species resemble one another.

Similar data was generated in the Dd2 strain and these showed comparable trends to NF54 with some minor differences (Fig. 4). First, the percent hemoglobin in Dd2 showed more variability and was larger than NF54 in the earlier trophozoite stage, resulting in a slightly larger overall percent of hemoglobin ($3.5 \pm 0.2\%$ vs $1.1 \pm 0.1\%$) and lower percent of heme ($6.1 \pm 0.2\%$ vs $7.9 \pm 0.2\%$) compared to NF54 (Fig. 4B, D). Interestingly, the maximum absolute amount of hemoglobin was also higher in Dd2 compared with NF54 (2.4 ± 0.4 vs 1.3 ± 0.2 fg/cell) and maximum absolute heme levels were lower (5.8 ± 0.9 vs 9.5 ± 0.6 fg/cell). Furthermore, the Dd2 curves for hemozoin and total iron increased exponentially across the entire 24-h period, without showing a decreased steepness between 36 and 44 h as was observed in NF54 (Fig. 4G, H).

Heme detoxification insights

Comparative analysis. Given that the PMs and heme-containing species examined localize to the DV, additional calculations were made to investigate the relative concentrations (as opposed to absolute amounts) of the soluble species within the NF54 DV lumen, i.e., the amounts of the PMs, hemoglobin and heme divided by the DV lumen volume measured herein (Figs. 3D and 5A). The hemozoin, although within the DV, does not occupy lumen space and was therefore excluded from this analysis. Notably, during the NF54 mid trophozoite stage (28 to 40 h), the relative concentration of the soluble species remained constant across timepoints. On the other hand, the relative concentrations of these species were comparably higher during the early trophozoite phase (20 to 28 h) and the schizont stage (40 to 48 h). Similar calculations were applied to Dd2, and it was found that between 20 and 32 h the relative concentrations of hemoglobin and heme were lower compared to the period between 32 and 40 h.

To further probe the degradation of hemoglobin, the amount of total Fe minus the remaining hemoglobin fraction was calculated (Fig. 5B). This metric corresponds to the amount of hemoglobin digested in femtograms (i.e., the heme plus hemozoin fractions). The gradient of the line therefore indicates the rate of hemoglobin digestion in femtograms per hour. Between 20 to 28 h, 28 to 40 h and 40 to 44 h, the rates were 1.3 fg/h, 5.1 fg/h and 1.7 fg/h, respectively, in NF54. Interestingly, in Dd2 parasites only two distinct phases were observed between 20 to 29 h and 29 to 44 h with digestion rates of 0.9 fg/h and 4.8 fg/h.

Discussion

The broad aim of this work was to probe important DV-related features that affect hemoglobin catabolism in its native state in *P. falciparum* parasites. In turn, this provided a deeper understanding of the underlying parasite biology involved in the heme detoxification pathway. Four crucial pieces of data were analyzed across the trophozoite to schizont life stage: (i) the growth of the DV lumen volume, (ii) the uptake into the DV, (iii) the levels of PM I and PM IV proteases and (iv) the basal levels of hemoglobin, heme and hemozoin in untreated parasites.

It was found that the growth of the DV lumen best fit a Gompertz growth curve during the early-to-late trophozoite stage before collapsing during the schizont stage in both NF54 and Dd2 strains (Fig. 2B). At the resolution of the confocal microscopy experiments used (Fig. 2A), accurate volumetric analysis of the pre-DV acidic cytosomal invaginations^{14–18} was not feasible. Thus, data was not collected between 0 and 20 h, and the assumption was made that the growth would follow the fitted curve during this period starting at (0,0). The uptake of pHrodo™ into the DV followed a comparable trend with the lumen volume, with the total uptake increasing dramatically from the early trophozoites to the late trophozoite stage, and then decreasing within the schizont stage (Fig. 2C), while the concentration of pHrodo remained constant (Fig. 2D). This indicates that lumen growth and uptake are tightly correlated, such that as the lumen grows, the parasite takes up more material leading to a constant pHrodo™ concentration within the vacuole.

Although the mechanism by which cytosomes fuse to the DV remains unclear⁵⁷, our hypothesis on why a sigmoidal-type growth of the lumen and uptake exists in both strains is based on the underlying biology of the parasite postulated by Tilley and colleagues that during the late ring stage, acidic, endocytic pre-DV vacuoles fuse to initiate DV biogenesis¹⁶. If one were to approximate the DV by a sphere, the volume would be calculated as: $V = \frac{4}{3}\pi r^3$, while the surface area would be calculated as: $SA = 4\pi r^2$, where r is the radius of the sphere. This indicates that the volume, which is dependent on r^3 , would grow faster than the r^2 -dependent surface area. In the context of the DV, the surface area would limit how quickly the volume grows because the surface of the DV provides the contact point for fusion of new vesicles. The larger the surface area, the more vesicles can fuse and therefore the larger the DV can grow. Between 0 and 20 h, the parasite is present in the ring phase, and therefore, the pre-exponential phase seen towards this asymptote is likely attributed to the limited surface area available as the small individual vesicles combine to form the central DV compartment seen in the trophozoite stage. This period (0 to 20 h) also corresponds to a lag in uptake which reflects the relatively low metabolic energy demand of the ring stage.

The growth phase between 20 and 36 h, and 20 and 32 h in the NF54 and Dd2 strains, respectively, corresponds to the trophozoite stage of the parasite. During this stage, the numerous small pre-DV vesicles continue fusing with the central DV compartment. The addition of each small vesicle in 3D space results in an ever-increasing surface area and therefore rapid volume growth, giving rise to the exponential-phase Gompertz growth and uptake curves. Notably, this lumen growth phase after 20 h corresponds to the most metabolically active stage of the parasite⁵⁸, correlating with the need for the rapid increase in uptake of RBC cytosol and large increase in lumen volume. As the energy demand of the parasite decreases and the majority of the hemoglobin from the RBC cytosol has been digested, the uptake and the growth begin to slow down resulting in the curve reaching its upper asymptote. This asymptote is visible in Dd2 for both the growth and uptake, but NF54 does not appear to reach an asymptote before the DV lumen begins to collapse. One possible explanation for this difference is that the Dd2 DV grows faster than that of NF54, thus reaching a point where the volume to expand is limited sooner than in NF54. It therefore approaches the upper asymptote more gradually as space within the RBC becomes limited.

As the parasites develop into the schizont stage at approximately 36 to 40 h in both strains, the DV lumen begins to collapse. This does not preclude the existence of the DV, rather the data suggests that during this schizont

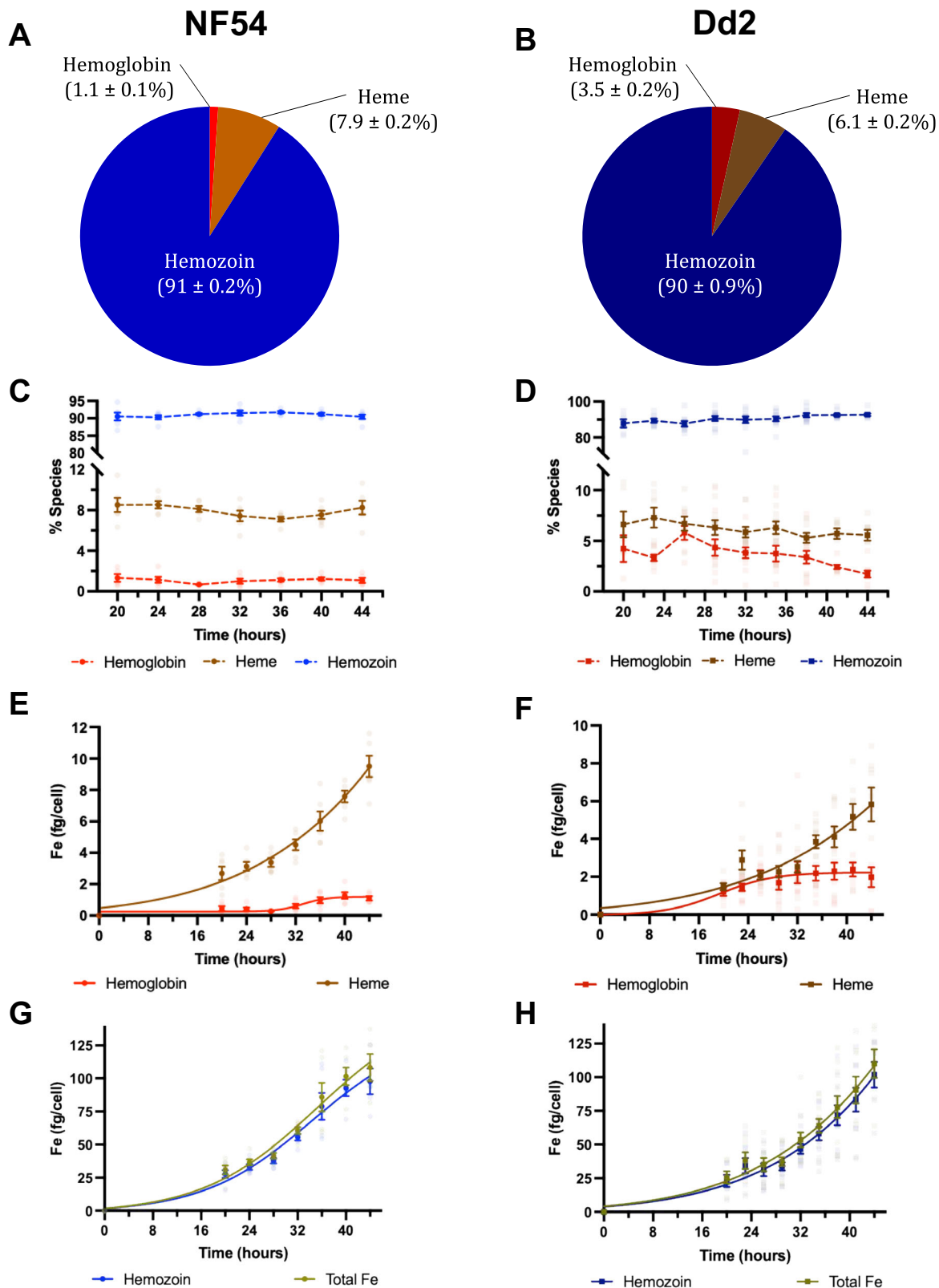


Fig. 4 | Time dependent cellular fractionation for describing the basal percent and absolute amounts of the heme-containing species over the trophozoite to schizont phases in NF54 and Dd2. The overall percent average of each heme-containing species across all timepoints (A, B). Percent heme-containing species

over time (C, D). Using flow cytometry counts, the absolute amounts in fg/cell were calculated of hemoglobin and heme (E, F), hemozoin and total Fe (G, H). For each data point $n \geq 6$ (from two independent repeats), error bars indicate SEM.

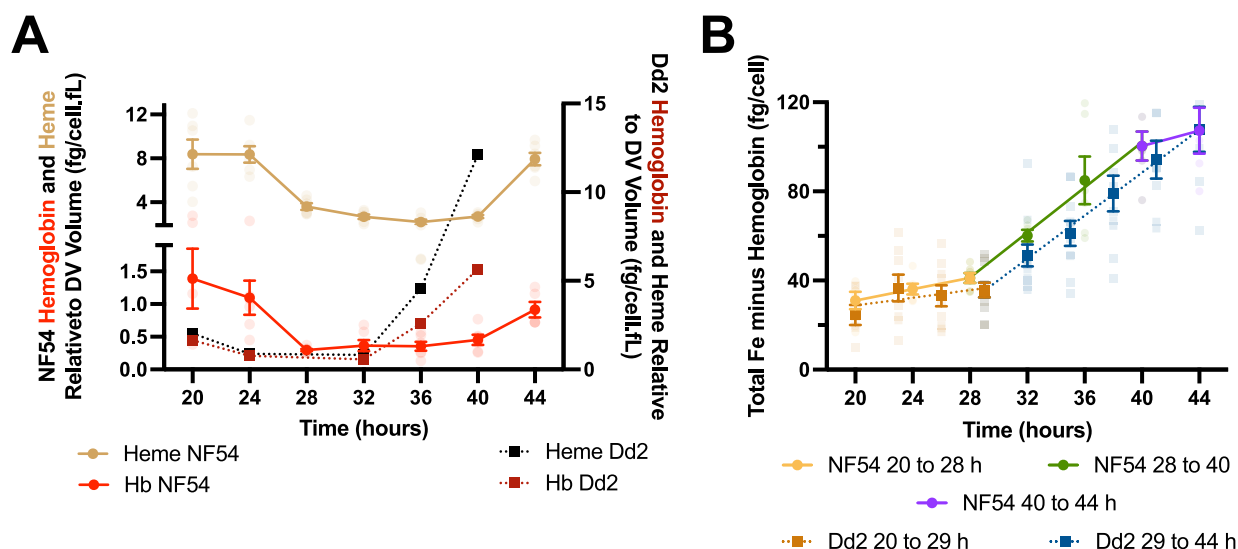


Fig. 5 | Comparative analysis of the residual hemoglobin, heme levels and digested hemoglobin in NF54 and Dd2. A The amounts of hemoglobin and heme obtained from the heme fractionation experiments (Fig. 4E, F), respectively, normalized to the DV lumen volume (Fig. 2B) in both NF54 (circles, shown on left y-axis) and Dd2 (squares, shown on right y-axis). These axes represent the relative

concentration of each species. **B** The amount of hemoglobin digested calculated as the total Fe minus the absolute hemoglobin fraction in NF54 parasites obtained in the heme fractionation experiments (Fig. 4E–H). For each data point $n \geq 6$ (from two independent repeats), error bars indicate SEM.

phase, the DV mainly consists of hemozoin crystals and very little inter-membrane space (compare T36 and T44, Fig. 2A, and T36 and T40, Supplementary Fig. 3A). Further evidence for the final collapse of the lumen can be seen in the schizont TEM image (Fig. 2B, Schizont Inset), which contains merozoites and shows the hemozoin crystals tightly wrapped in the DV membrane (white arrow). This residual membrane-wrapped hemozoin is left behind when the schizonts burst to release merozoites and can be observed as debris under a light microscope.

A previous study has shown that the total DV volume, which includes hemozoin crystals, of the wild-type HB3 and drug-resistant Dd2 strains follows a sigmoidal growth pattern⁴². While the shape of the Dd2 growth curve herein agrees with the previous study, the observed absolute volumes differ⁴². The maximum total volume of the Dd2 DV, including hemozoin crystals, was previously shown to reach ~5.5 fL in the late-trophozoite stage (30 h), while the volume for the Dd2 DV lumen in our study was shown to reach 3.7 fL at a similar stage (32 h), a difference of 1.8 fL. This variance is likely attributed to the volume occupied by the hemozoin crystals, which are excluded in the current measurements and appear from this analysis to occupy almost a third of the DV at this time point. Furthermore, the previous study did not present data beyond 30 h and therefore the collapse of the DV lumen was not studied. The collapse, which manifests as a decrease in the amount of aqueous space (lumen) within the DV, has not been studied before, and therefore the mechanism by which this happens is unclear. Our hypothesis is that, in light of the fact that the growth of the total DV volume reaches a plateau in the late trophozoite, while hemozoin continues to accumulate^{42,59}, the growth kinetics of the hemozoin crystals overtake the growth kinetics of the DV, leading to hemozoin taking over the available lumen space within the DV, resulting in the observed lumen collapse. Although there are number of possibilities for the fate of the lumen contents, it appears that PM I and PM IV are simply left behind in the residual DV as energy is diverted away from hemoglobin metabolism towards merozoite formation (Fig. 3E, F).

Interestingly, it was observed that the volume of the lumen in Dd2 was larger than in NF54 across all timepoints, similar to previous observations made between the total DV volumes of drug-sensitive and resistant strains^{42,60–62}. These studies attributed the observed difference to *PfCRT* mutations. The association of *PfCRT* mutations with altered vacuolar volume was previously confirmed using a CQS strain transfected with

mutant *PfCRT*, C3^{Dd242}. This isogenic edited *PfCRT* mutant showed increases in DV volume comparable to Dd2 relative to an unmodified CQ sensitive laboratory strain, GCO3, implicating the direct or indirect involvement of *PfCRT*⁴². Recent observations that the native function of *PfCRT* involves transport of key substrates (such as peptides), which appears to be impaired in mutant *PfCRT*, supports its role in causing larger vacuoles in drug-resistant parasites relative to drug-sensitive parasites^{63–65}. Indeed, this study suggests that the increased total DV volume observed in *PfCRT* mutants is as a result of increased lumen volume and not merely more hemozoin. Thus, the impaired function of mutant *PfCRT* may cause peptides that would otherwise be exported to accumulate within the DV lumen of Dd2 parasites resulting in the increased lumen. Additionally, we observed that Dd2 parasites have a higher basal level of hemoglobin than NF54 (Fig. 4A–F), suggesting that the Dd2 lumen contains more hemoglobin at any given time compared to NF54. Therefore, one hypothesis is that the inhibited transport of substrates by mutant *PfCRT* in Dd2 not only leads to larger vacuoles, but causes a shift in the equilibrium between the digested vs undigested hemoglobin, relative to NF54^{42,66}. These observations may also be a key factor in the earlier collapse of the Dd2 lumen compared to the NF54 lumen, and have been implicated in previous studies as an explanation for reduced fitness. More specifically, piperazine resistant parasites with reduced fitness have enlarged DV lumens which have been attributed to the accumulation of peptides⁶⁰. Thus, the change in the equilibrium of hemoglobin digestion may also play a role in parasites with reduced fitness.

For further insights and a holistic view of the heme detoxification process, the inter-strain levels of all the heme-containing species within the DV were investigated. When looking at the overall percentage of each species over the entire stage (Fig. 4A, B), it appears that in general Dd2 parasites not only had a higher percentage of hemoglobin, but also a lower percentage of heme compared to NF54 parasites, while the percentage of hemozoin was comparable between the strains. Additionally, it was interesting to note that although heme has been shown to be toxic to the parasite^{67,68}, it can tolerate seemingly non-toxic levels as the DV lumen volume expands, since the total heme concentration remains below 13 fg of heme Fe per fL (Fig. 5A) or 0.233 M.

While the percentage of each heme-containing species remained steady over the trophozoite to schizont life stage, a time-dependent increase in the absolute values of all species was observed in both NF54 and

Dd2 strains to varying degrees (Fig. 4). Prior to 20 h, ring stage parasites cannot adequately pellet during centrifugation to give heme-species data points and therefore the absolute level graphs were interpolated with the point (0,0) and extrapolated using this point between 0 and 20 h. The biological basis of the interpolation of this point is that merozoites have been shown to contain an inactive cytosomal ring on their periphery, indicating that parasite feeding has not yet commenced at this stage^{14,69}. This extrapolation results in a gradual increase in heme-containing species defined by the curve fit between 0 and 20 h, corresponding to the ring stage. The extrapolation of the hemoglobin fraction is supported by the presence of active cytosomes during the ring stage, allowing the parasite to begin feeding on the RBC cytosol in the pre-trophozoite phase⁷⁰. Support for the extrapolation of the heme and hemozoin curves, lies in the fact that previous studies have documented the presence of pre-DV, acidic vacuoles that begin to form during the ring stage which have been shown to contain hemozoin, substantiating the catabolism of hemoglobin in the early ring stage^{16,71,72}. Naturally, these factors would in turn support the extrapolation of the total Fe curve.

The absolute hemoglobin levels remained within a narrow range in both NF54 and Dd2, while the heme, hemozoin and total Fe levels showed exponential increases to varying degrees (Fig. 4E–H). A more complete picture of the pathway emerges when the percent and absolute amounts are considered holistically and in combination with the DV lumen volume (Fig. 5A). In general, there is an interdependence between the growth of the DV lumen volume and the absolute amounts of the heme-containing species such that the proportion of each species (Fig. 4C, D) remains approximately constant. This, coupled with the fact that the heme concentration remains below 233 mM, indicates a tightly regulated homeostasis of these species that the parasite maintains throughout the trophozoite to schizont life stage.

Notably, in NF54, the total Fe over the 24-h period (Fig. 4G) and the uptake of pHrodo into the DV (Fig. 2C) corroborate each other. In NF54, from 20 to 40 h the amount of RBC cytosol taken up and total Fe increases exponentially, after which the DV collapses, less cytosol is taken in and the rate of increase in the total Fe begins to slow (Figs. 2C and 4G). This is unsurprising given that the source of the heme-derived Fe in the parasite is derived predominantly from hemoglobin uptake and digestion⁷³. In Dd2, however, although uptake into the DV plateaus before decreasing (Fig. 2C), the total Fe increases exponentially over the same period (Fig. 4H), further supporting the disruption caused by *PfCRT* mutations to processes in the DV, relative to the wild-type. A noteworthy observation is that the low levels of hemoglobin and gradual increase in total Fe over time do not support one of the modes of uptake previously suggested termed the “big gulp”¹⁸. Rather the data support the reliance on cytosomal invaginations as the primary method of uptake in line with other previous findings that have also contradicted the big gulp theory^{14,16–18,72,74,75}.

An interesting basis for how hemoglobin is processed in wild-type parasites is provided by a holistic examination of the data. Over the trophozoite to schizont stage (28 to 40 h) a tight homeostasis of hemoglobin degradation and the heme detoxification process is maintained in NF54 parasites (Fig. 5A). On either side of this stage, in early trophozoite (20 to 28 h) and early-to-late schizont (40 to 48 h), there appears to be higher relative concentration of the PMs (Fig. 3D), hemoglobin and heme (Fig. 5A), however, there also appears to be a slower rate of hemoglobin catabolism compared to the mid-trophozoite stage (Fig. 5B). During these periods the DV lumen is at its smallest and correlates with stages when the parasite and therefore, the DV, are transitioning between different phases, i.e., from ring to trophozoite in the early stage and from trophozoite to schizont in the latter. During the mid trophozoite stage (28 to 40 h), the relative concentration of the soluble material appears to be lower, but constant, while the hemoglobin degradation rate appears to be higher. This correlates with the period in which the parasite is most metabolically active and reliant on hemoglobin degradation and heme detoxification. Most interestingly, regardless of the phase, the proportion of the hemoglobin, heme and hemozoin relative to each other remains constant.

In Dd2, a slightly different pattern is observed. It appears that rather than three distinct phases, there are two. The earlier-to-mid trophozoite stage (20 to 32 h) correlates with lower relative concentrations of hemoglobin and heme (Fig. 5A), as well as a lower rate of hemoglobin degradation (20 to 29 h, Fig. 5B). The relative hemoglobin and heme concentrations then increase past 32 h correlating with a higher rate of hemoglobin degradation. Despite these observed differences, similar to NF54, the proportions of the heme-containing species remain fairly constant.

When considering all the parameters studied, these data contribute to a holistic overview of the heme detoxification pathway which provides a deeper understanding of the fundamental biology of the DV. A theoretical DV physiology schematic for NF54 and Dd2 are shown in Fig. 6 and provide insights into these parasite strains. Included in this figure is a summary of the data presented in this manuscript. The picture of the NF54 DV that emerges is one that is characterized by three distinct growth periods: (1) lag-type growth (20 to 28 h), (2) rapid growth (28 to 40 h), and (3) the plateau (40 to 48 h).

During the lag-type growth (20 to 28 h) the lumen volume, uptake into the DV and levels of heme, hemozoin and total Fe increase gradually. An interesting feature of this growth period is the relatively higher concentration of the soluble matter within the DV compared to later stages. It is unclear why the concentration level of the soluble matter would be elevated compared to the later stages; however, this may be due to a concentrating of the soluble matter within a relatively smaller DV and a hallmark of a transition period of the parasite DV. The rate of hemoglobin degradation is lowest during this phase.

The lag-type growth period is followed by the rapid growth period (28 to 40 h) which is characterized by a significant increase in the DV lumen volume, uptake and levels of each heme-containing species. This corresponds to the most metabolically active stage of the intraerythrocytic parasite life cycle with the largest contribution to overall ABS parasite growth, where increased hemoglobin catabolism allows for the preservation of intracellular osmotic pressure^{35,36}. During this mid-trophozoite phase there are higher relative protein levels of PM I and PM IV compared to the earlier phase, which would allow for the processing of increasing amounts of hemoglobin, however, a steady state concentration of these proteins maintains the constant concentration of hemoglobin. Finally, this growth phase is characterized by a higher rate of hemoglobin degradation compared to the earlier or later stages.

The final phase, the plateau (40 to 48 h), is distinguished by a collapse of the DV lumen and a linear decrease of the uptake into the DV. The decreased uptake is reflected in the slowing increase of the levels of hemozoin and total Fe in NF54. The heme levels on the other hand continue to follow the exponential curve trajectory, presumably as a result of continued hemoglobin degradation. At this point in the life cycle, the parasite has grown to a size that takes up most of the space within the RBC and therefore, its dependence on hemoglobin uptake becomes inconsequential, and parasite resources are diverted towards schizogony and merozoite formation leading to a lower rate of hemoglobin degradation. During this phase, it appears that the PMs are concentrated within the shrinking DV. The penultimate fate of the DV is a residual body of “shrink-wrapped” hemozoin crystals and residual aqueous matter.

In contrast, although the growth of and uptake into the Dd2 DV follows a similar trend to the NF54 DV, the underlying hemoglobin degradation characteristics indicate two distinct phases: (1) phase one (20 to 29 h) and (2) phase two (29 to 46 h). During the first phase, the relative concentration of soluble matter remains lower compared to the latter phase, while the increase in the heme-containing species is gradual. Interestingly, the DV lumen grows most rapidly during this phase and begins to plateau. During the second phase, the heme-containing species, except hemoglobin, increase dramatically accompanied by large increases in the relative concentration of the soluble species. The DV lumen volume also collapses during this phase from 32 h. Finally and most pertinent to the two phases, the rate of hemoglobin degradation appears to be lower during the first phase and higher during the second. Overall, these differing

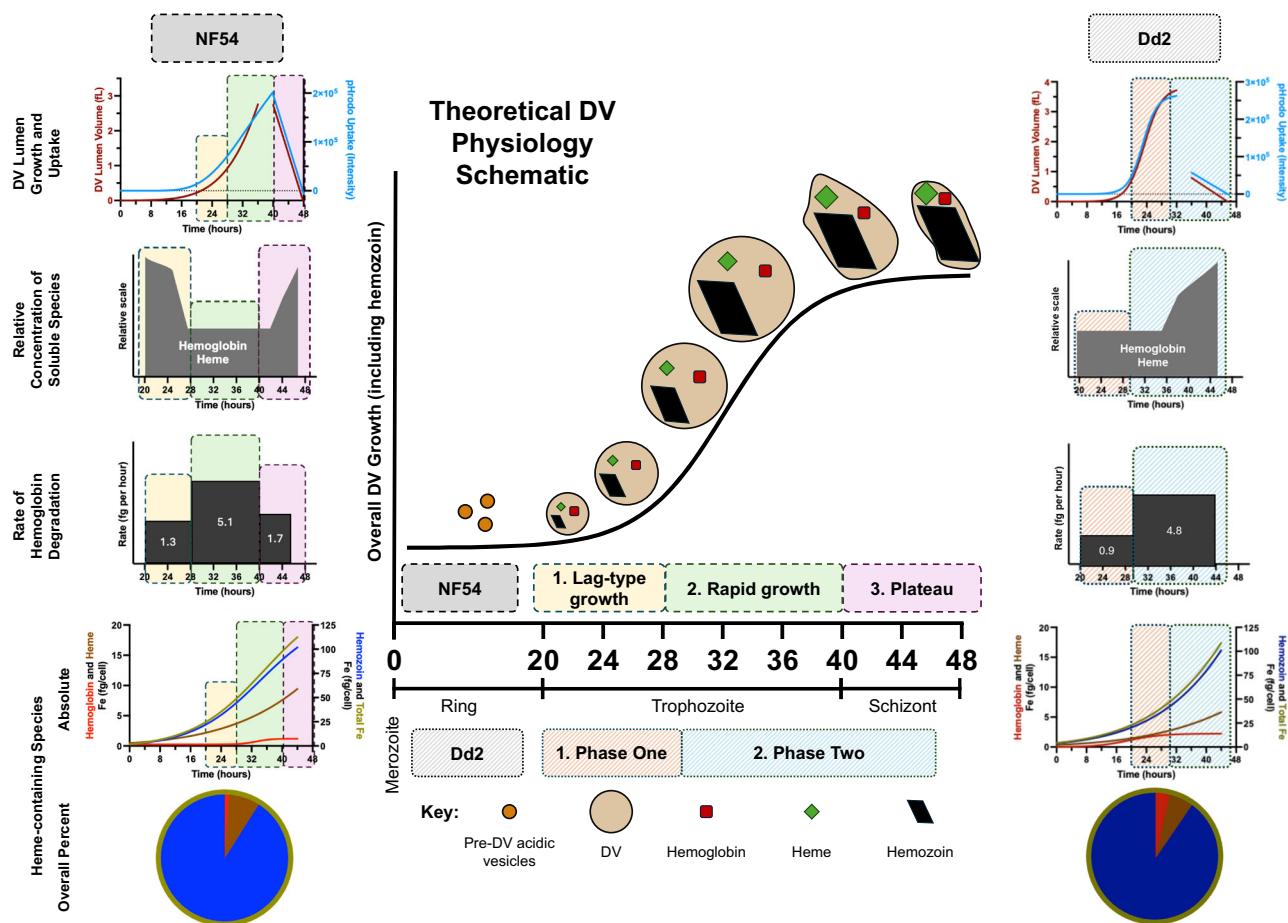


Fig. 6 | Proposed DV physiology of NF54 and Dd2 parasites. Summary of the experimental data acquired of the heme detoxification pathway and schematic of the proposed DV physiology showing the growth phases for NF54 and Dd2 parasites.

observations support the observations that *PfCRT* mutations in Dd2 parasites affect hemoglobin processing relative to wild-type parasites, although these differences may also be related to or influenced by parasite background and origin.

This study presents a more holistic overview of the physiology of the malaria parasite DV, an important organelle and site of action of numerous clinical and experimental antimalarial drugs. Given that important ACT partner drugs and compounds in development target hemozoin formation, understanding the mechanics of this pathway remain imperative. This study also highlights some of the strain differences between wild-type NF54 and CQ-resistant Dd2 strains in terms of DV lumen volume, uptake into the DV and basal levels of heme species over time. Thus, the continued study of the heme detoxification pathway and DV physiology may lead to a basis for an improved understanding of resistance mechanisms. Indeed, these acquired data provide a platform and framework to extend the current knowledge of DV physiology and thus, beckons the continued study of this vital pathway at a basal level between different drug-resistant parasite strains. Finally, understanding how pathway inhibitors affect hemoglobin processing is equally important and will allow for specific parts of the pathway to be further probed.

Methods

Cell culture

General method. *Plasmodium falciparum* parasites were maintained in continuous culture based on the Trager and Jensen method⁷⁶. Briefly, parasites were maintained in complete medium (10.4 g/L RPMI-1640, 4.0 g/L glucose, 0.088 g/L hypoxanthine, 6.0 g/L HEPES, 5.0 g/L Albumax II, 0.05 g/L Gentamycin and 2.25 g/L sodium bicarbonate) and O⁺ red

blood cells obtained from the Western Cape Blood Services, Cape Town, at 5% parasitemia and 2% hematocrit. Ring stage parasites were synchronized by treatment with 5% sorbitol⁷⁷.

Preparation of cultures for time-sensitive assays. All *Plasmodium* cell lines were sourced, with thanks, from the Fidock Lab, Columbia University Irving Medical Centre, New York, USA. In preparation for time-sensitive assays, parasite cultures were monitored closely to track parasite and kept tightly synchronized for at least one week prior to experimental set-up. For NF54 parasites, cultures were synchronized within two ranges in consecutive 48-h life cycle periods, at either 0 to 4 h or 14 to 18 h post merozoite invasion. For Dd2 parasites, cultures were synchronized twice within the same 46-h life cycle at 0 to 4 h or 14 to 18 h post merozoite invasion.

Percoll® gradient enrichment. A 5× RPMI/25% sorbitol solution was used to dilute pure Percoll® to the required concentration. The Percoll® gradient enrichment was performed by layering 600 μL of 60% Percoll® on top of an equal volume of 90% Percoll® in an Eppendorf tube. Of the pRBC pellet, 200 μL was then layered on the top and the samples spun down in a microfuge at 750 rcf for 10 min.

Flow cytometry. In general, trophozoites were isolated using saponin lysis by gently mixing a 0.15% saponin lysis buffer in PBS and a pRBC pellet in approximately a 1:10 ratio. Upon the solution becoming a translucent red color, it was centrifuged at 750 rcf and the supernatant aspirated. The resultant trophozoite pellet was then washed two to three times with 1× PBS and subsequently dissolved in 1× PBS. The

trophozoites were then fixed by addition to a counting diluent (0.125% v/v glutaraldehyde and 0.5% v/v DNase I) in a 1:10 ratio and the samples stored at 4 °C for no more than three days prior to running on the flow cytometer. Samples were prepared for flow cytometry by adding together FACS diluent (1× SYBR® Green solution), BD™ Trucount® bead solution (1 mL filtered PBS added to a tube of Trucount® beads and vortexed) and the fixed sample in an 8:1:1 ratio. The samples were then incubated at 37 °C for 30 min and run on a BD™ C6 CSampler flow cytometer at medium fluidics with sample collection limited to 50 µL or 100 µL. All files were exported as FACS files and saved for processing in FlowJo™ (v9 to v10) Software (BD Life Sciences)⁷⁸.

Digestive vacuole studies

RBC loading⁴². RBCs were washed with complete media and then 500 µL added to 1 mL of pre-warmed hypotonic solution (5 mM HEPES, 11 mM glucose and 2 mM NaATP). To produce pHrodo™ loaded RBCs, to the hypotonic solution 50 µL of 1 mg/mL pHrodo™ dextran (Invitrogen, P10361) stock was added to produce a final concentration of 50 µg/mL. Control RBCs were produced using unmodified hypotonic solution. The hypotonic solutions containing the RBCs were then incubated at 37 °C for 10 min, after which 1 mL of pre-warmed hypertonic solution (300 mM NaCl, 40 mM KCl and 11 mM glucose) was added to create an overall isotonic solution to promote resealing of the RBC membrane. The resealed RBCs were then washed three times with culture medium and used immediately after preparation.

Incubation and harvesting. To a 50 mL cell culture flask, 50 µL of a 5% parasitemia pRBC pellet, 200 µL of the resealed RBCs (either containing or not containing pHrodo™) and 13 mL culture medium were added. The flasks were gassed with mixed air and incubated at 37 °C for the required incubation period to achieve certain parasite ages. Following incubation, cultures were spun down and the supernatant aspirated. For NF54 parasites, of the pellet, 5 µL was used to prepare a Giemsa slide blood smear, 200 µL was enriched using Percoll® gradient enrichment and the remainder was saponin lysed, fixed and processed for flow cytometry as described above the following working day. The enriched sample was harvested for confocal imaging at the 60%/90% interface and washed twice with PBS. For Dd2 parasites, cultures were not enriched, instead 5 µL of the pellet was used to prepare a Giemsa slide blood smear and 50 µL of the pellet was saponin lysed, fixed and processed for flow cytometry. The remainder of the pRBC pellet was used for confocal sample preparation. Of the enriched NF54 pellet or Dd2 pRBC pellet, 5 µL was added to 2 mL of Ringer's solution⁴⁰ (122.5 mM NaCl, 5.4 mM KCl, 1.2 mM CaCl₂, 0.8 mM MgCl₂, 11.0 mM glucose, 25.0 mM HEPES and 1.0 mM NaH₂PO₄) containing Hoechst stain (ThermoFisher, H3570, 1:5000) to produce the final sample for confocal imaging.

Confocal imaging. Either single- or four-chambered CellView™ dishes were coated with filtered 0.01% poly-L-lysine and dried at 37 °C prior to use. To the single chamber CellView™ dishes, 500 µL of the confocal sample was added, while 200 µL of the confocal sample was added to the four chamber CellView™ dishes. This was allowed to settle for 5 min before the excess liquid was aspirated. To prevent samples from drying out, fresh Ringer's solution was gently added to the chambers to not disturb the settled cells. Samples were imaged using a Zeiss Confocal Microscope LSM 880, AxioObserver (Airyscan). Settings were established during the first experiment and then reused for every subsequent experiment to ensure consistency across different experiments. A C Plan-Apochromat 63× Oil Objective was used with an effective NA of 1.4 and the scan zoom was set to 8.5. The pHrodo™ signal was detected using the red channel (570 to 600 nm band pass filter) while Hoechst was detected using the blue channel (385 to 420 nm band pass filter). The pinhole size for the pHrodo™ channel was 2.31 Airy Units (AU) and the detector gain was set to 700. For Hoechst, the pinhole size was 3.20 AU and the detector gain was set to 850. Using the Z-stack function in Zen Black (Zeiss),

Z-stacks of individual parasites were acquired and subsequently subjected to Airyscan processing. The original files in their .czi format were transferred to a storage device and then saved on OneDrive. All samples were imaged within 6 h of sample collection to ensure sample integrity.

Image analysis. The files were processed in Zen Blue Lite (Zeiss) to produce 3D renderings and images for documents. The volume, uptake and concentration analyses were performed using ImageJ^{45,46}. The Fiji (Fiji Is Just ImageJ) package was downloaded and installed from the ImageJ website. The .czi files were imported into ImageJ using the Bio-Formats Plugin⁷⁹ and the color channels separated. The red channel Z-stacks were then subjected to a threshold using the built-in RenyiEntropy automatic threshold. The volume analysis was conducted in two ways. In one instance, the “Analyze Particles” (AP) built-in function on ImageJ was used in which the calculations were limited to the threshold and the circularity set to 0.05 to infinity. The resultant area of each region of interest were then summed in Excel and multiplied by the Z-stack spacing to obtain the volume. In the second instance, the 3D Objects Counter Plugin (3D OC)⁴⁷ was used to calculate the volume by applying the RenyiEntropy automatic threshold to the Z-stack using the stack histogram and subsequently applying the 3D OC function to the resultant Z-stack after applying the threshold. All the volume data was then collated and compared in Microsoft Excel and analyzed using GraphPad Prism (v8 to v10, GraphPad Software Inc, USA)⁸⁰. To determine the uptake and concentration of the DV, the raw integrated density was obtained for each Z-stack from the file generated by the AP function. The uptake was determined to be the summation of the integrated density of each Z-stack. To calculate the concentration, this value was divided by the volume calculated for that individual parasite.

PM I and IV protein analysis

Parasite lysate preparation. The saponin lysis protocol was adopted to isolate the NF54 trophozoites. Additionally, trophozoites isolated from Dd2 PM I and PM IV KO lines were used as controls to confirm specificity of the antibodies. PM KO lines were generated from a Dd2 parental line using a pHD-22y vector system that relies on a human dihydrofolate reductase as the selectable marker as described previously⁵². To the isolated trophozoite pellets, 45 µL filtered PBS was added, the solutions were mixed thoroughly and 5 µL of the cell suspension was added to 45 µL of counting diluent. The fixed samples were processed for flow cytometry as described above in 96-well plates and used to calculate the cell concentration. To the remaining 40 µL of the isolated trophozoite cell suspension, 10 µL of 5× sample application buffer (SAB, 5% β-mercaptoethanol solution in 5× SDS running buffer) was added. The samples were mixed thoroughly and heated at 90 °C for 5 min using a heating block. The samples were then stored at –20 °C until further use. All samples needed for the SDS-PAGE were diluted with 1× SAB to a final volume of 10 µL such that 50,000 parasites were contained in the lysate.

SDS-PAGE. All back- and spacer plates (casting plates) were washed and cleaned with 70% EtOH prior to use. SDS-PAGES consisting of 12% resolving gel (12% acrylamide/bis-acrylamide 37:1, 375 mM Tris pH 8.8, 0.1% w/v SDS, 0.05% v/v TEMED, 0.1% w/v ammonium persulphate) and 5% stacking gel (5% acrylamide/bis-acrylamide 37:1, 250 mM Tris pH 6.8, 0.1% SDS w/v, 0.1% v/v TEMED, 0.1% w/v ammonium persulphate) at 1 mm thickness and containing 15 lanes were hand-cast using a Bio-Rad Mini-Protean 3 casting chamber. Page gels not used immediately were wrapped airtight in cling wrap and stored at 4 °C. Stored page gels were used within 24 h of casting. A Bio-Rad Mini-Protean Tetra System electrophoresis tank was filled with 1× SDS running buffer (25 mM Tris, 250 mM glycine and 0.5% w/v SDS) and assembled with the page gel. The sample wells were flushed with 1× SDS running buffer prior to loading and to each well 10 µL of parasite lysate or 3 µL NEB Color Prestained Protein Standard Broad Range (P7719S, 10–250 kDa) were added according to a predetermined loading pattern. The electrophoresis

was run for 45 to 60 min at a constant current of 30 mA per gel and variable voltage. Page gels were removed and immediately processed for the western transfer.

Western blot preparation. A PVDF membrane was activated for 15 s in MeOH and then placed in 1× western transfer buffer (25 mM Tris, 250 mM glycine and 10% v/v MeOH) along with the other components needed for the blotting cassette to equilibrate for 5 min. The blotting cassette was then assembled as per the manufacturer guidelines and placed into the electrophoresis tank which was then filled with 1× western transfer buffer. The transfer was run for 1 h and 40 min at a constant voltage of 100 V and variable current. Once completed, the PVDF membrane was washed three times with 1× TBST (20 mM Tris pH 8.0, 150 mM NaCl and 0.1% Tween® 20) for 5 min and transferred to blocking buffer (5% w/v skim milk solution in TBST) for 40 min. Once blocked, the membrane was incubated with primary antibody solutions overnight at 4 °C with gentle shaking. All *Plasmodium* antibodies were sourced, with thanks, from the Fidock Lab, Columbia University Irving Medical Centre, New York, USA. These were primarily sourced from Dr Daniel E. Goldberg, Howard Hughes Medical Institute and Department of Medicine and Molecular Microbiology, Washington University School of Medicine, St. Louis, MO as per Omara-Opyene et al.⁵⁵. Anti-PM I (rabbit, 1: 10,000), anti-PM IV (mouse, 1:10,000) and anti-BiP (rabbit, 1:20,000) were all prepared using blocking buffer. Following incubation with the primary antibodies, the membrane was washed three times with 1× TBST for 5 min and treated with horse radish peroxidase (HRP)-conjugated secondary anti-rabbit (Merck cat. A0545-1ML, 1:3000) or anti-mouse (Merck cat. A4416-1ML, 1:3000) antibodies for 1 h with gentle shaking. The membranes were then washed three times with TBST for 5 min. The Advanta WesternBright® Sirius® detection kit was used for signal detection. Briefly, the PVDF membrane was treated for 2 min with 1 mL of a 1:1 ratio mixture of luminol/enhancer solution and peroxide chemiluminescent detection reagent. Any excess solution was removed, and the membrane secured in cling wrap in a light-proof X-ray cassette. In a dark room, the signal was detected by exposure to X-ray film, which were subsequently developed, fixed, and rinsed with tap water. Once dry, the X-ray films were scanned using an Epson Perfection V800 scanner using Epson Scan Software and stored in the .tiff format.

Densitometric blot analysis. Scanned blots were imported into ImageJ and analyzed as previously described⁵⁶. Briefly, .tiff files were converted to gray scale 8-bit images and a background 8-bit image created using the “Subtract Background” function with “Create background – don’t subtract” activated and the rolling ball radius set to 50.0 pixels. Using the “Image Calculator”, the background image was subtracted from the original 8-bit image to generate a negative image that was then inverted using the “Look Up Tables” (LUT) to generate an image with a white background and dark foreground pixels. The blot was then analyzed using the “Gels” function to produce histograms for each band. These were then quantified using the “Wand” tool and the data acquired as arbitrary area values. Using the “Label Peaks” function, the fractional area of each band was obtained relative to each other. The raw data were then exported into Excel and GraphPad Prism for further analysis.

Immunofluorescence assays (IFA)

Sample preparation. From an NF54 parasite culture of mixed age at 5–8% parasitemia and 3% hematocrit, 1 mL was pelleted by centrifugation. All spins were conducted at 1500 rpm for 2 min in a tabletop centrifuge. The parasite pellet was washed with 1× PBS and fixed in 4% formaldehyde and 0.0075% glutaraldehyde for 20 min at room temperature (RT). Following a wash with 1× PBS, the cells were permeabilized with 0.1% Triton X-100 for 20 min at RT and washed again with 1× PBS. To block any non-specific binding sites, the cells were incubated with 3% bovine serum albumin (BSA) on a tube rotator for 3 h at 4 °C. Following centrifugation and removal of the 3% BSA, fresh 3% BSA was

added, and dilutions of the antibodies were added as follows to different samples: anti-PM I (rabbit, 1:2000) and anti-CRT (mouse, 1:300)⁹ or anti-PM IV (mouse, 1:500). The samples were then incubated overnight at 4 °C on a tube rotator. The cells were then washed with 0.1% Tween in 1× PBS twice for 15 min at 4 °C with rotation. Secondary antibodies were then added to the appropriate samples to detect the primary antibody. The antibodies used were goat anti-rabbit Alexa Fluor 647 (ThermoFisher, A-21247, PM I detection), goat anti-mouse Alexa Fluor 488 (ThermoFisher, A-21121, CRT detection) and goat anti-mouse Alexa Fluor 647 (ThermoFisher, A-21235, PM IV detection). The samples were incubated with rotation at 4 °C for 2 h and the washes with 0.1% Tween in 1× PBS repeated to remove any unbound secondary antibody. Samples were then incubated in Hoechst (1:500 in 1× PBS) for 20 min at 4 °C with rotation and washed once with 1× PBS. The pellet size was then assessed and an equal volume of 1× PBS was added to the pellet. Of this, 2.5 µL was smeared on a poly-L-lysine coated slide and allowed to dry in the dark. Once dry, 2 µL Vectashield® (Vector Laboratories, H-1900-2) antifade mounting media was added to the slide and a cover slip secured over the smear with sealant. Slides were stored at 4 °C in the dark until imaging.

Confocal imaging. Samples were imaged using a Zeiss Confocal Microscope LSM 900. Settings were established during the first experiment and then reused for every subsequent experiment to ensure consistency across different experiments. A C Plan-Apochromat 63× Oil Objective was used with an effective NA of 1.4 and the scan zoom was set to 5. The Hoechst signal was detected using the blue channel (348 to 455 nm band pass filter), CRT was detected in the green channel (493 to 517 nm band pass filter), and PM I/PM IV were detected in the far red channel (653 to 668 nm band pass filter) Using the Z-stack function in Zen Black (Zeiss), Z-stacks of individual parasites were acquired on the confocal setting. The original files in their .czi format were transferred to a storage device and then saved on OneDrive. Images were then viewed and processed using ZEN blue software.

Basal levels of the heme-containing species³⁷

Incubation and harvesting. NF54 parasites at 4% parasitemia, 2% hematocrit and 2 mL culture volume were incubated in flat-bottomed 12-well plates (Greiner) in an airtight gas chamber flushed with mixed air at 37 °C for variable incubation periods. Dd2 parasites were prepared at 3% parasitemia, 2% hematocrit and 6 mL culture volume in flat-bottomed 6-well plates (Greiner). Following the required incubation period for harvesting parasites at a given age, excess media supernatant was aspirated, and Giemsa-stained thin smears were prepared and visually analyzed to assess any changes to the parasite population. The pellets were resuspended in 1.8 mL 1× PBS and transferred to deep-well 2.2 mL 96-well plates (Greiner). To this, 125 µL 1% saponin was added and following gentle shaking for 2 min, the plates were centrifuged for 15 min at 750 rcf and the supernatant aspirated. The isolated trophozoite pellets were washed two to three times with 0.5 mL 1× PBS followed by a 15 min centrifugation at 750 rcf after each wash to remove all erythrocyte hemoglobin. The isolated trophozoites were then resuspended in 100 µL filtered 1× PBS and accurately transferred to a round-bottomed, 96-well 0.5 mL plate (Axygen) referred to as the “stock plate”. Of this, 10 µL was transferred to a flat-bottomed 96-well plate (Greiner) containing 190 µL counting diluent. This plate was referred to as the “counting plate”. The stock plate and counting plate were then stored at –20 °C and 4 °C, respectively, until further use. The counting plate was then processed for flow cytometry as described above to determine cell count.

Cellular fractionation. Following thawing of the stock plate, 100 µL of MilliQ water (mH₂O) was added to each well and the plate sonicated for 5 min in an ultrasound bath. To this, 50 µL 0.2 M HEPES buffer (pH 7.5) was added, and the plate centrifuged at 3600 rpm for 20 min. Carefully, without disturbing the pellet, the supernatant was transferred to an adjacent set of wells on the same plate. To the supernatant, 50 µL 4% w/v

SDS was added, the plate sonicated for 5 min and incubated at RT for 30 min. Following incubation, 50 μ L 0.3 M NaCl and 50 μ L 25% v/v pyridine (25% v/v in 0.2 M HEPES pH 7.5) in 0.2 M HEPES (pH 7.5) were added and 200 μ L of this solution transferred to a flat-bottomed, 96-well plate termed the “reading plate”. This fraction corresponded to the hemoglobin fraction.

The pellet was treated with 50 μ L mH₂O and 50 μ L 4% SDS and resuspended well. The plate was sonicated for 5 min and incubated at RT for 30 min. Following incubation, 50 μ L each of 0.2 M HEPES (pH 7.5), 0.3 M NaCl and 25% pyridine were added, and the plate centrifuged at 3600 rpm for 20 min. Without disturbing the delicate pellet, the supernatant was transferred to an adjacent set of well on the same plate. The supernatant was diluted to 400 μ L with mH₂O and 200 μ L of this solution was transferred to the reading plate. This fraction corresponded to the heme fraction.

The remaining pellet was treated with 50 μ L 0.3 M NaOH and 50 μ L mH₂O, the plate sonicated for 15 min and incubated at RT for 30 min. To this, 50 μ L each of 0.2 M HEPES (pH 7.5), 0.3 M HCl and 25% pyridine was added, and finally, 150 μ L of mH₂O. Of this, 200 μ L was transferred to the reading plate. The UV-visible spectra of heme as an Fe(III)PPIX-(bis)pyridyl complex was recorded between 400 and 415 nm on a multi-well plate reader (ThermoScientific MultiskanGO). The absorbance maxima of each well were used to calculate the absolute amount and percentage of each heme-containing species in each sample.

Heme standard curve. The absolute amount of each heme-containing species was quantified using a heme standard curve. A 100 μ g/mL standard solution of hematin (porcine) in 0.3 M NaOH was prepared and 200 μ L added to a round-bottomed, 96-well plate (Axygen). Serial dilutions of the standard solution were carried out across the plate using 100 μ L 0.3 M NaOH, leaving a blank column for reference. Of each of the following solutions, 50 μ L were added to 100 μ L of hematin standard: 0.2 M HEPES (pH 7.5), 4% w/v SDS, 0.3 M NaCl, 0.3 M HCl, 25% v/v pyridine in 0.2 M HEPES (pH 7.5) and mH₂O. The UV-visible spectra of heme as the Fe(III)PPIX-(bis)pyridyl complex from 400 to 415 nm were recorded using a multi-well plate reader. The standard curve was used to calculate the absolute amount of each heme-containing species as Fe (fg/mL) using the following equation:

$$M_{\text{Fe}} = M_{\text{H}} \times \left(\frac{MW_{\text{Fe}}}{MW_{\text{H}}} \right)$$

M_{Fe} = mass of Fe, M_{H} = mass of hematin, MW_{Fe} = molecular mass of Fe, and MW_{H} = molecular mass of hematin.

Statistics and reproducibility

General. In general, “N” in the manuscript refers to independent biological replicates. The definition of “n” depends on the type of experiment, for the imaging experiments “n” refers to individual parasites, while in other experiments “n” refers to technical replicates. For statistical analyses, unpaired student *t*-tests were used. For graph fitting, GraphPad Prism software was used.

Reporting summary

Further information on research design is available in the Nature Portfolio Reporting Summary linked to this article.

Data availability

All data supporting the findings of this study are available within the paper and the Supplementary Information. The raw experimental data are available in Figshare with the identifier <https://doi.org/10.6084/m9.figshare.28801805>⁸¹. Additional data are available from the corresponding author upon reasonable request.

Received: 7 April 2025; Accepted: 2 October 2025;

Published online: 13 November 2025

References

- World malaria report addressing inequity in the global malaria response. *Geneva: World Health Organization*; 2024. Licence: CC BY-NC-SA 3.0 IGO (2024).
- Moss, S. et al. How has mass drug administration with dihydroartemisinin-piperazine impacted molecular markers of drug resistance? A systematic review. *Malar. J.* **21**, 1–23 (2022).
- Report on antimalarial drug efficacy, resistance and response: 10 years of surveillance (2010–2019). *Geneva: World Health Organization*; Licence: CC BY-NC-SA 3.0 IGO (2020).
- Rosenthal, P. J. et al. The emergence of artemisinin partial resistance in Africa: how do we respond?. *Lancet Infect. Dis.* **24**, e591–e600 (2024).
- Dziwornu, G. A. et al. 2, 8-Disubstituted-1, 5-naphthyridines as dual inhibitors of *Plasmodium falciparum* phosphatidylinositol-4-kinase and hemozoin formation with in vivo efficacy. *J. Med. Chem.* **67**, 11401–11420 (2024).
- Amod, L., Mohunlal, R., Teixeira, N., Egan, T. J. & Wicht, K. J. Identifying inhibitors of β -haematin formation with activity against chloroquine-resistant *Plasmodium falciparum* malaria parasites via virtual screening approaches. *Sci. Rep.* **13**, 2648 (2023).
- Okombo, J. et al. Pyrido-dibemequine metabolites exhibit improved druglike features, inhibit hemozoin formation in *Plasmodium falciparum*, and synergize with clinical antimalarials. *ACS Infect. Dis.* **9**, 653–667 (2023).
- Daniel, L. et al. Metal (triphenylphosphine)-Atovaquone complexes: synthesis, antimalarial activity, and suppression of heme detoxification. *Inorg. Chem.* **63**, 17087–17099 (2024).
- Murithi, J. M. et al. The *Plasmodium falciparum* ABC transporter ABCI3 confers parasite strain-dependent pleiotropic antimalarial drug resistance. *Cell Chem. Biol.* **29**, 824–839. e826 (2022).
- Horatscheck, A. et al. Identification of 2, 4-disubstituted imidazopyridines as hemozoin formation inhibitors with fast-killing kinetics and in vivo efficacy in the *Plasmodium falciparum* NSG mouse model. *J. Med. Chem.* **63**, 13013–13030 (2020).
- Dhingra, S. K. et al. A variant PfCRT isoform can contribute to *Plasmodium falciparum* resistance to the first-line partner drug piperazine. *MBio* **8**, e0030317 (2017).
- Fidock, D. A. et al. Mutations in the *P. falciparum* digestive vacuole transmembrane protein PfCRT and evidence for their role in chloroquine resistance. *Mol. Cell* **6**, 861–871 (2000).
- Sidhu, A. B. S., Verdier-Pinard, D. & Fidock, D. A. Chloroquine resistance in *Plasmodium falciparum* malaria parasites conferred by pfcrt mutations. *Science* **298**, 210–213 (2002).
- Aikawa, M., Hepler, P. K., Huff, C. G. & Sprinz, H. The feeding mechanism of avian malarial parasites. *J. Cell Biol.* **28**, 355–373 (1966).
- Lazarus, M. D., Schneider, T. G. & Taraschi, T. F. A new model for hemoglobin ingestion and transport by the human malaria parasite *Plasmodium falciparum*. *J. Cell Sci.* **121**, 1937–1949 (2008).
- Bakar, N. A., Klonis, N., Hanssen, E., Chan, C. & Tilley, L. Digestive-vacuole genesis and endocytic processes in the early intraerythrocytic stages of *Plasmodium falciparum*. *J. Cell Sci.* **123**, 441–450 (2010).
- Milani, K. J., Schneider, T. G. & Taraschi, T. F. Defining the morphology and mechanism of the hemoglobin transport pathway in *Plasmodium falciparum*-infected erythrocytes. *Eukaryot. Cell* **14**, 415–426 (2015).
- Elliott, D. A. et al. Four distinct pathways of hemoglobin uptake in the malaria parasite *Plasmodium falciparum*. *Proc. Natl Acad. Sci. USA* **105**, 2463–2468 (2008).
- Francis, S. E. et al. Molecular characterization and inhibition of a *Plasmodium falciparum* aspartic hemoglobinase. *EMBO J.* **13**, 306–317 (1994).
- Banerjee, R. et al. Four plasmepsins are active in the *Plasmodium falciparum* food vacuole, including a protease with an active-site histidine. *Proc. Natl Acad. Sci. USA* **99**, 990–995 (2002).

21. Goldberg, D. E., Slater, A., Cerami, A. & Henderson, G. B. Hemoglobin degradation in the malaria parasite *Plasmodium falciparum*: an ordered process in a unique organelle. *Proc. Natl Acad. Sci. USA* **87**, 2931–2935 (1990).
22. Goldberg, D. E. et al. Hemoglobin degradation in the human malaria pathogen *Plasmodium falciparum*: a catabolic pathway initiated by a specific aspartic protease. *J. Exp. Med.* **173**, 961–969 (1991).
23. Francis, S. E., Gluzman, I. Y., Oksman, A., Banerjee, D. & Goldberg, D. E. Characterization of native falcipain, an enzyme involved in *Plasmodium falciparum* hemoglobin degradation. *Mol. Biochem. Parasitol.* **83**, 189–200 (1996).
24. Shenai, B. R., Sijwali, P. S., Singh, A. & Rosenthal, P. J. Characterization of native and recombinant falcipain-2, a principal trophozoite cysteine protease and essential hemoglobinase of *Plasmodium falciparum*. *J. Biol. Chem.* **275**, 29000–29010 (2000).
25. Rosenthal, P. J., McKerrow, J., Aikawa, M., Nagasawa, H. & Leech, J. A malarial cysteine proteinase is necessary for hemoglobin degradation by *Plasmodium falciparum*. *J. Clin. Investig.* **82**, 1560–1566 (1988).
26. Gamboa de Dominguez, N. & Rosenthal, P. J. Cysteine proteinase inhibitors block early steps in hemoglobin degradation by cultured malaria parasites. *Blood* **87**, 4448–4454 (1996).
27. Eggleston, K. K., Duffin, K. L. & Goldberg, D. E. Identification and characterization of falcilysin, a metallopeptidase involved in hemoglobin catabolism within the malaria parasite *Plasmodium falciparum*. *J. Biol. Chem.* **274**, 32411–32417 (1999).
28. Wang, F. et al. Biochemical characterization of *Plasmodium falciparum* dipeptidyl aminopeptidase 1. *Mol. Biochem. Parasitol.* **175**, 10–20 (2011).
29. Klemba, M., Gluzman, I. & Goldberg, D. E. A *Plasmodium falciparum* dipeptidyl aminopeptidase I participates in vacuolar hemoglobin degradation. *J. Biol. Chem.* **279**, 43000–43007 (2004).
30. Kolakovich, K. A., Gluzman, I. Y., Duffin, K. L. & Goldberg, D. E. Generation of hemoglobin peptides in the acidic digestive vacuole of *Plasmodium falciparum* implicates peptide transport in amino acid production. *Mol. Biochem. Parasitol.* **87**, 123–135 (1997).
31. Dalal, S. & Klemba, M. Roles for two aminopeptidases in vacuolar hemoglobin catabolism in *Plasmodium falciparum*. *J. Biol. Chem.* **282**, 35978–35987 (2007).
32. Teuscher, F. et al. The M18 aspartyl aminopeptidase of the human malaria parasite *Plasmodium falciparum*. *J. Biol. Chem.* **282**, 30817–30826 (2007).
33. de Villiers, K. A. & Egan, T. J. Heme detoxification in the malaria parasite: a target for antimalarial drug development. *Acc. Chem. Res.* **54**, 2649–2659 (2021).
34. Krugliak, M., Zhang, J. & Ginsburg, H. Intraerythrocytic *Plasmodium falciparum* utilizes only a fraction of the amino acids derived from the digestion of host cell cytosol for the biosynthesis of its proteins. *Mol. Biochem. Parasitol.* **119**, 249–256 (2002).
35. Lew, V. L., Macdonald, L., Ginsburg, H., Krugliak, M. & Tiffert, T. Excess haemoglobin digestion by malaria parasites: a strategy to prevent premature host cell lysis. *Blood Cells Mol. Dis.* **32**, 353–359 (2004).
36. Lew, V. L., Tiffert, T. & Ginsburg, H. Excess hemoglobin digestion and the osmotic stability of *Plasmodium falciparum*-infected red blood cells. *Blood* **101**, 4189–4194 (2003).
37. Combrinck, J. M. et al. Optimization of a multi-well colorimetric assay to determine haem species in *Plasmodium falciparum* in the presence of anti-malarials. *Malar. J.* **14**, 1–14 (2015).
38. Bailly, C. Pyronaridine: An update of its pharmacological activities and mechanisms of action. *Biopolymers* **112**, e23398 (2021).
39. Vanaerschot, M. et al. Hexahydroquinolines are antimalarial candidates with potent blood-stage and transmission-blocking activity. *Nat. Microbiol.* **2**, 1403–1414 (2017).
40. Kuhn, Y., Rohrbach, P. & Lanzer, M. Quantitative pH measurements in *Plasmodium falciparum*-infected erythrocytes using pHluorin. *Cell. Microbiol.* **9**, 1004–1013 (2007).
41. Tilley, L., Dixon, M. W. & Kirk, K. The *Plasmodium falciparum*-infected red blood cell. *Int. J. Biochem. Cell Biol.* **43**, 839–842 (2011).
42. Gligorijevic, B., Bennett, T., McAllister, R., Urbach, J. S. & Roepe, P. D. Spinning disk confocal microscopy of live, intraerythrocytic malarial parasites. 2. Altered vacuolar volume regulation in drug resistant malaria. *Biochemistry* **45**, 12411–12423 (2006).
43. NIAID Visual & Medical Arts. (10/10/2025). Eppendorf Tube. NIAID NIH BIOART Source. <http://bioart.niaid.nih.gov/bioart/143>.
44. NIAID Visual & Medical Arts. (10/10/2025). Low Friction Flask. NIAID NIH BIOART Source. <http://bioart.niaid.nih.gov/bioart/303>.
45. Schindelin, J. et al. Fiji: an open-source platform for biological-image analysis. *Nat. Methods* **9**, 676–682 (2012).
46. Schneider, C. A., Rasband, W. S. & Eliceiri, K. W. NIH Image to ImageJ: 25 years of image analysis. *Nat. Methods* **9**, 671–675 (2012).
47. Ollion, J., Cochenne, J., Loll, F., Escude, C. & Boudier, T. TANGO: a generic tool for high-throughput 3D image analysis for studying nuclear organization. *Bioinformatics* **29**, 1840–1841 (2013).
48. Sakaguchi, M., Miyazaki, N., Fujioka, H., Kaneko, O. & Murata, K. Three-dimensional analysis of morphological changes in the malaria parasite infected red blood cell by serial block-face scanning electron microscopy. *J. Struct. Biol.* **193**, 162–171 (2016).
49. Rudlaff, R. M., Kraemer, S., Marshman, J. & Dvorin, J. D. Three-dimensional ultrastructure of *Plasmodium falciparum* throughout cytokinesis. *PLoS Pathog.* **16**, e1008587 (2020).
50. Gompertz, B. XXIV. On the nature of the function expressive of the law of human mortality, and on a new mode of determining the value of life contingencies. *Philos. Trans. R. Soc. Lond.* **115**, 513–583 (1825).
51. Winsor, C. P. The Gompertz curve as a growth curve. *Proc. Natl Acad. Sci. USA* **18**, 1–8 (1932).
52. Bonilla, J. A. et al. Effects on growth, hemoglobin metabolism and paralogous gene expression resulting from disruption of genes encoding the digestive vacuole plasmepsins of *Plasmodium falciparum*. *Int. J. Parasitol.* **37**, 317–327 (2007).
53. van Dooren, G. G. et al. Development of the endoplasmic reticulum, mitochondrion and apicoplast during the asexual life cycle of *Plasmodium falciparum*. *Mol. Microbiol.* **57**, 405–419 (2005).
54. Russo, I., Oksman, A., Vaupel, B. & Goldberg, D. E. A calpain unique to alveolates is essential in *Plasmodium falciparum* and its knockdown reveals an involvement in pre-S-phase development. *Proc. Natl Acad. Sci.* **106**, 1554–1559 (2009).
55. Omara-Opyene, A. L. et al. Genetic disruption of the *Plasmodium falciparum* digestive vacuole plasmepsins demonstrates their functional redundancy. *J. Biol. Chem.* **279**, 54088–54096 (2004).
56. Gallo-Oller, G., Ordóñez, R. & Dotor, J. A new background subtraction method for Western blot densitometry band quantification through image analysis software. *J. Immunol. Methods* **457**, 1–5 (2018).
57. Spielmann, T., Gras, S., Sabitzki, R. & Meissner, M. Endocytosis in *Plasmodium* and *Toxoplasma* parasites. *Trends Parasitol.* **36**, 520–532 (2020).
58. Olszewski, K. L. & Llinás, M. Central carbon metabolism of *Plasmodium* parasites. *Mol. Biochem. Parasitol.* **175**, 95–103 (2011).
59. Gligorijevic, B., McAllister, R., Urbach, J. S. & Roepe, P. D. Spinning disk confocal microscopy of live, intraerythrocytic malarial parasites. 1. Quantification of hemozoin development for drug sensitive versus resistant malaria. *Biochemistry* **45**, 12400–12410 (2006).
60. Ross, L. S. et al. Emerging Southeast Asian PfCRT mutations confer *Plasmodium falciparum* resistance to the first-line antimalarial piperazine. *Nat. Commun.* **9**, 3314 (2018).
61. Wicht, K. J., Small-Saunders, J. L., Hagenah, L. M., Mok, S. & Fidock, D. A. Mutant PfCRT can mediate piperazine resistance in African *Plasmodium falciparum* with reduced fitness and increased

- susceptibility to other antimalarials. *J. Infect. Dis.* **226**, 2021–2029 (2022).
62. Small-Saunders, J. L. et al. Evidence for the early emergence of piperazine-resistant *Plasmodium falciparum* malaria and modeling strategies to mitigate resistance. *PLoS Pathog.* **18**, e1010278 (2022).
 63. Shafik, S. H. et al. The natural function of the malaria parasite's chloroquine resistance transporter. *Nat. Commun.* **11**, 3922 (2020).
 64. Okombo, J. et al. Piperazine-resistant PfCRT mutations differentially impact drug transport, hemoglobin catabolism and parasite physiology in *Plasmodium falciparum* asexual blood stages. *PLoS Pathog.* **18**, e1010926 (2022).
 65. Hagenah, L. M. et al. Additional PfCRT mutations driven by selective pressure for improved fitness can result in the loss of piperazine resistance and altered *Plasmodium falciparum* physiology. *Mbio* **15**, e01832–01823 (2024).
 66. Bennett, T. N. et al. Drug resistance-associated pfCRT mutations confer decreased *Plasmodium falciparum* digestive vacuolar pH. *Mol. Biochem. Parasitol.* **133**, 99–114 (2004).
 67. Chou, A. & Fitch, C. Hemolysis of mouse erythrocytes by ferriprotoporphyrin IX and chloroquine. Chemotherapeutic implications. *J. Clin. Investig.* **66**, 856–858 (1980).
 68. Kumar, S. & Bandyopadhyay, U. Free heme toxicity and its detoxification systems in human. *Toxicol. Lett.* **157**, 175–188 (2005).
 69. Bannister, L. & Mitchell, G. The role of the cytoskeleton in *Plasmodium falciparum* merozoite biology: an electron-microscopic view. *Ann. Trop. Med. Parasitol.* **89**, 105–111 (1995).
 70. Bannister, L., Hopkins, J., Fowler, R., Krishna, S. & Mitchell, G. A brief illustrated guide to the ultrastructure of *Plasmodium falciparum* asexual blood stages. *Parasitol. Today* **16**, 427–433 (2000).
 71. Dluzewski, A. R. et al. Formation of the food vacuole in *Plasmodium falciparum*: a potential role for the 19 kDa fragment of merozoite surface protein 1 (MSP119). *PLoS ONE* **3**, e3085 (2008).
 72. Grüning, C. et al. Development and host cell modifications of *Plasmodium falciparum* blood stages in four dimensions. *Nat. Commun.* **2**, 165 (2011).
 73. Egan, T. J. et al. Fate of haem iron in the malaria parasite *Plasmodium falciparum*. *Biochem. J.* **365**, 343–347 (2002).
 74. Wunderlich, J., Rohrbach, P. & Dalton, J. P. The malaria digestive vacuole. *Front. Biosci.-Scholar* **4**, 1424–1448 (2012).
 75. Sojka, D., Jalovecká, M. & Perner, J. Theileria, *Plasmodium* and Hemoglobin. *Microorganisms* **10**, 1651 (2022).
 76. Trager, W. & Jensen, J. B. Human malaria parasites in continuous culture. *Science* **193**, 673–675 (1976).
 77. Lambros, C. & Vanderberg, J. P. Synchronization of *Plasmodium falciparum* erythrocytic stages in culture. *J. Parasitol.* **65**, 418–420 (1979).
 78. Becton & Dickson. *FlowJo(TM) Software (for Windows) [FlowJo v10.8]* (BD Life Sciences, 2023).
 79. Bankhead, P. Analyzing fluorescence microscopy images with ImageJ. *ImageJ* **1**, 10.1109 (2014).
 80. GraphPad Prism versions. 8.0.0 to 10.0.0 for Windows (GraphPad Software, USA).
 81. Garnie, L. Heme processing in the malaria parasite, *Plasmodium falciparum*: a time-dependent basal-level analysis_raw data [Dataset]. *Figshare* <https://doi.org/10.6084/m9.figshare.28801805.v3>. (2025).

Acknowledgements

This research is dedicated to the late Professor Timothy Egan. The study was funded by the National Institute of Allergy and Infectious Diseases of the National Institutes of Health under Award Number 5R01AI143521. The content of this publication is solely the responsibility of the authors and does not necessarily represent the official views of the National Institutes of

Health. We thank Prof. David Fidock and the Fidock Lab from Columbia University Irving Medical Center for donating the Dd2 plasmepsin I and IV knockout lines and plasmepsin antibodies, as well as access to their laboratory and resources to conduct the IFAs. Notably, we would like to thank Dr Kharizta Wiradiputri from the Fidock Lab for her expertise and training in IFAs. We would like to also thank Dr Thomas Oelgeschläger and Dr Jasmin Knopp from the Faculty of Molecular and Cell Biology at the University of Cape Town for the contribution of their expertise and training in western blot techniques, as well as the access to their laboratory and resources to conduct the research. We thank Dr Joanne Egan for the use of her TEM images in Fig. 2. We also thank Dr Jill Combrinck for her expertise and training in the cell fractionation assay and Dr Katherine de Villiers for her assistance in reviewing some of the data in this manuscript. We would like to thank Dr Dirk Lang and Susan Cooper at the Confocal and Light Microscopy Imaging Facility at the University of Cape Town for training provided in confocal microscopy.

Author contributions

L.F.G.: Conceptualization, investigation, analysis, writing original draft, reviewing and editing. T.J.E.: Funding acquisition, conceptualization, supervision. K.J.W.: Funding, supervision, writing, reviewing and editing.

Competing interests

The authors declare no competing interests.

Additional information

Supplementary information The online version contains supplementary material available at <https://doi.org/10.1038/s42003-025-08991-z>.

Correspondence and requests for materials should be addressed to Kathryn J. Wicht.

Peer review information *Communications Biology* thanks Leann Tilley and the other, anonymous, reviewer(s) for their contribution to the peer review of this work. Primary Handling Editors: Nishith Gupta and Tobias Goris. A peer review file is available.

Reprints and permissions information is available at <http://www.nature.com/reprints>

Publisher's note Springer Nature remains neutral with regard to jurisdictional claims in published maps and institutional affiliations.

Open Access This article is licensed under a Creative Commons Attribution-NonCommercial-NoDerivatives 4.0 International License, which permits any non-commercial use, sharing, distribution and reproduction in any medium or format, as long as you give appropriate credit to the original author(s) and the source, provide a link to the Creative Commons licence, and indicate if you modified the licensed material. You do not have permission under this licence to share adapted material derived from this article or parts of it. The images or other third party material in this article are included in the article's Creative Commons licence, unless indicated otherwise in a credit line to the material. If material is not included in the article's Creative Commons licence and your intended use is not permitted by statutory regulation or exceeds the permitted use, you will need to obtain permission directly from the copyright holder. To view a copy of this licence, visit <http://creativecommons.org/licenses/by-nc-nd/4.0/>.

© The Author(s) 2025